# Chapter 4: Dynamic damage and fracture processes in brittle materials

Pascal Forquin

# Chapter 4: Dynamic damage and fracture processes in brittle materials

P. Forquin, Univ. Grenoble Alpes, G-INP, CNRS, Lab. 3SR, pascal.forquin@univ-grenoble-alpes.fr

## Abstract

Brittle materials such as, rocks, concrete and high-performance concrete, glass, ceramics, ice..., are materials abundantly present in our everyday life and materials involved in many industrial applications or in various protective solutions. Achieving a good understanding of their strain-rate sensitivity in relation with their microstructure remains a major issue. In addition, the development of micromechanics-based models is of major importance in view of improving the predictive capabilities of analytical and numerical models and in order to better explain the role of material parameters involved in the strain-rate and pressure sensitivity of brittle materials.
In the present chapter the damage and fracture processes involved in various brittle materials are discussed. Several experimental techniques offering the capability to characterize and analyse these damage modes are presented. Next, some micromechanics-based models attending to describe these mechanisms are detailed. Experimental and modelling approaches allow highlighting the main microstructural parameters driving the behaviour of brittle materials at high loading rates.

## 4.1 Brittle materials under extreme conditions: a host of industrial and societal challenges

Fragile, easily breakable, difficult to machine, expansive, low toughness, with unpredictable or non-determinist behaviour "brittle materials" do not have the best reputation in the world of industry or mechanical engineering. However, under extreme loading situations such as high temperatures, high confining pressures or dynamic loads, brittle materials may appear as very attractive in comparison with other materials such as metals, polymers or some composites. For instance, ceramics have been known since antiquity as heat-resistant materials and are widely used under high temperature conditions (Kingery et al., 1976). Indeed, the tensile or compressive strength of ceramics such as silicon carbide or alumina is seen to be virtually constant over a wide range of temperatures up to 1000 to 1200 K (Lankford, 1981; 1991). Industrial ceramics are also appreciated for their high hardness and low density in comparison with steel which makes them efficient in shielding configurations. The high compressive strength of ceramics leads to shattering of the projectile. A backing generally made of composite or metal then absorbs the kinetic energy of the fragments by plastic deformation. However, the ceramic itself undergoes intense damage and deformation modes (micro-plasticity, micro-cracking, multiple fragmentation…) that need to be analysed and better understood in order to optimize such shielding solutions.

Rock blasting is another important issue in geomechanics and civil engineering for building engineering structures such as roads, tunnels, bridges, or dams but also in open quarries to produce blocks, aggregates, and gravel. In such situations, fragmentation of rocks needs to be controlled to limit the extension of cracking, to obtain the required size of blocks, and to adjust as well as possible the quantity of explosives, their power, and the number and position of the charges. The distinct zones resulting from rock blasting were identified by Kutter and Fairhurst (1971), namely, a comminuted area (or crushing zone) in the vicinity of the explosive followed by a damaged zone in which dense microcracking is observed and finally a zone where few long cracks develop. Better understanding how inherent flaws may influence pore compaction, shearing processes and tensile fracturing remains a major issue (Grange et al, 2008). The percussive drilling method, commonly used in the tunnelling and mining industry, is another situation involving intense but localised pressures and high-rate tensile loading. The impact of a piston on the drill rod creates a stress wave that is transferred onto the rock through the tool buttons. The rock is then fragmented and flushed out by using water or air. Unlike the situation at quasi-static indentation, the stress waves and rapid indentation make percussive drilling a transient dynamic problem with high local strain rates in the rock (Saksala, 2010; Saadati et al, 2015; 2017).

Concretes remain the most used building materials thanks to their low cost and ease of casting. Understanding the dynamic response of concrete and cement-based materials is essential for designing structures that can withstand intense loading conditions, including civil, defence, and critical infrastructures. Concrete structures can be exposed to intense loadings such as contact detonation or rigid projectile impact leading to a complex transient dynamic loading characterised by high levels of confining pressure, strong deformation processes (shear and compaction) along with high-rate tensile loadings. In the case of projectile impact, typical failure modes are scabbing on the front face (i.e., conical cracks that emerge on the front surface), cracking around the tunnel region due to tensile hoop stresses generated by the swelling of the tunnel during projectile penetration, spalling on the rear face (i.e., conical cracks on the rear surface) due to axial punching of the projectile, microcracking parallel to the tunnel corresponding to shear deformation ahead of the projectile (confined compression in front of the projectile) (Forquin et al, 2006). A constitutive law able to describe both the plastic deformation under confinement of concrete and its anisotropic damage in tensile loading is essential for numerically simulating the response of concrete structures under ballistic impact (Forquin et al, 2015).

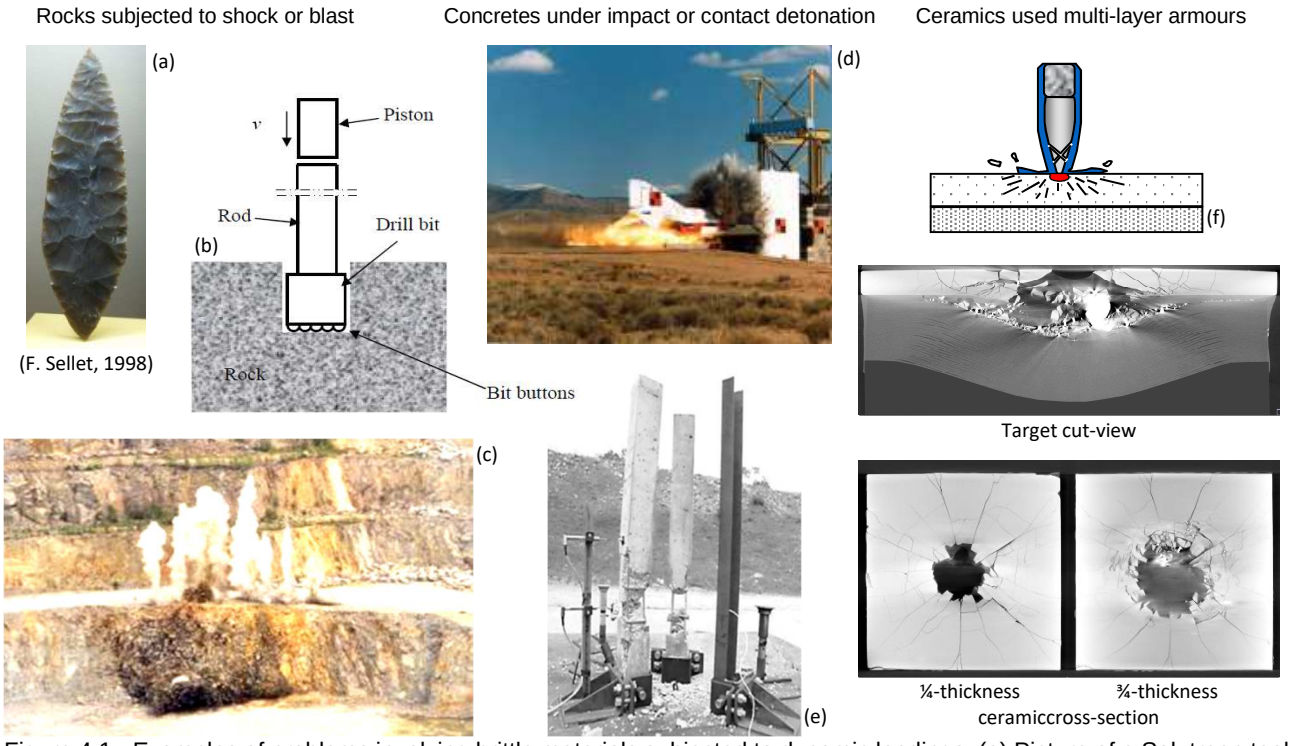


Figure 4.1 - Examples of problems involving brittle materials subjected to dynamic loadings. (a) Picture of a Solutrean tool (14,000 ybc), (b) Percussive drilling, (c) Rock blasting, (d) Impact against a concrete structure, (e) Contact detonation applied to concrete columns, (f) Impact of Armour-Piercing projectile (7.62 API-BZ) against a bilayer ceramic-composite armour, analysed with CT-scan microtomography.

The Figure 4.2 illustrates the damage modes induced in a target subjected to the impact of a small cylindrical projectile. The target is a mortar composed of fine sand (maximum size ≈ 500 µm), cement (Lafarge PEMS 52.5), silica fumes, water and additive silica fume with a water to (cement + binder) ratio reduced 0.41. The impact test was conducted with a cylindrical steel projectile (D5.3 mm, H8 mm, 1.2 g) of high hardness (65 HRC) fired at a speed of about 762 m/s. The target of dimensions 70x70x50 $mm^3$ was placed in an aluminum casing to restrict any movement of debris during the impact within the damaged block. After the impact, the block was infiltrated with a hyper-fluid colored resin, then cut, reinfiltrated and polished for inspection. Post-mortem fracturing pattern (Fig. 4.3) reveals an intense micro-cracking network around the tunnel where large pores, which are observed beyond this zone, seem to have disappeared. It is supposed that microcracking and pore collapse occurred in this area due to dynamic shearing and high confining pressure. In addition, numerous long cracks radiating from this first zone are observed. These cracks should result from tensile hoop stresses that spread out through the target during the penetration process. In addition, saucer-shaped cracks develop parallel to the impact surface before emerging on the top surface. This mode II cracking mode results from dynamic shearing leading to the target cratering.

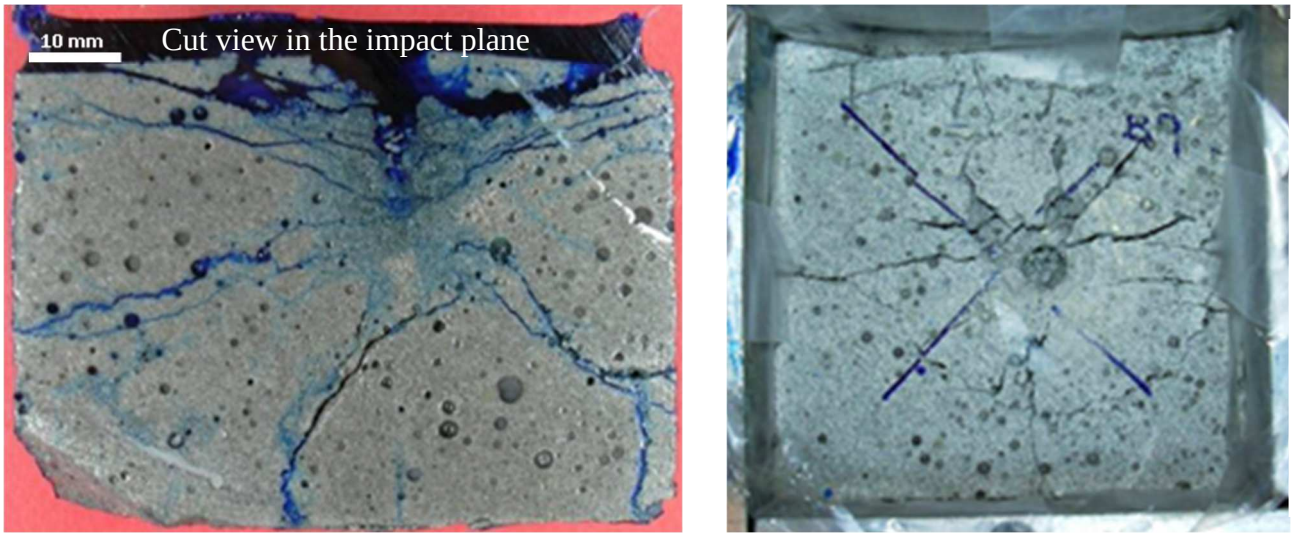


Figure 4.2 - Ballistic impact of small bullet against Mortar (Impact velocity: 762 m/s, depth of penetration: 14.9 mm) (Forquin et al, 2006).

In conclusion, the present introduction stresses that many kinds of brittle materials are subjected to extreme loading conditions involving high pressure levels or high-rate tensile and shear loadings depending on conditions of use. The sensitivity to pressure and strain-rate of such materials is discussed in the next subsection.

## 4.2 Brittle materials: scattering and size effect at low strain-rate, an introduction to the Weibull model

Under quasi-static tensile loading most brittle materials undergo brittle failure due to a single crack initiation event leading to the failure of the whole structure. This process is called single fragmentation in contrast to the multiple fragmentation process that occurs in brittle materials at high-rates. It follows that a weakest link hypothesis is made (Freudenthal, 1968) and a Weibull model (1951) can be used to fit experimental data. Figure 4.3 illustrates the result of 3-point bend tests performed with Ductal® concrete without fibres. The sample dimensions are L×h×b = 150×11×10 mm$^3$ and the span length is 130 mm. An elastic-brittle failure is observed along with a strong scatter in the failure stresses. In addition, as revealed by the failure patterns of several samples, flaws (large pores near the top side of fracture plane in Fig. 4.3) are responsible for crack initiation and the larger the pore size the lower the failure stress, which demonstrates that a relationship can be built between flaw properties and macroscopic behaviour.

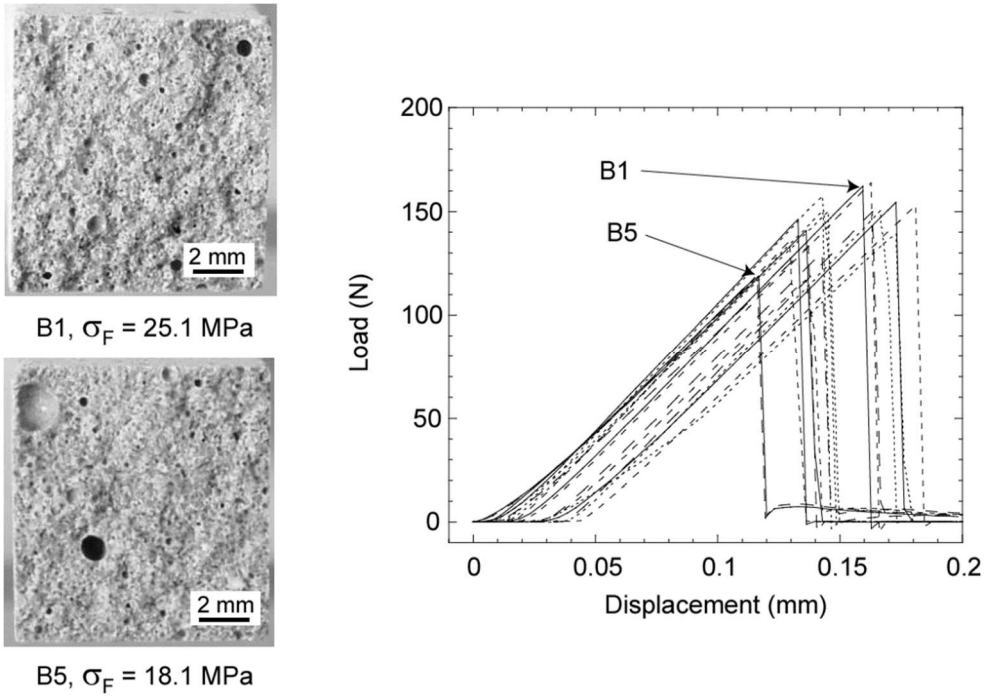


Figure 4.3 - Results of 3-point bend tests performed with an ultra-high-performance concrete (Ductal® without fibres) and two post-mortem observations.

The material can be assumed to contain point defects of density $\lambda_t$. Such hypotheses are those of a Poisson point process of intensity $\lambda_t$ (Gulino and Phoenix, 1991; Jeulin, 1991). Knowing the probability of finding $\delta$ critical defects within a uniformly loaded domain $\Omega$ of size $Z$:

$$P(\delta, \Omega) = \frac{(\Lambda_t)^\delta}{\delta!} exp(-\Lambda_t), \quad (1)$$

the probability of finding $\delta = 0$ critical defect reads:

$$P(0, \Omega) = exp(-\Lambda_t), \quad (2)$$

where $\Lambda_t$ corresponds to the average number of defects within $\Omega$. For a uniformly loaded domain, $\Lambda_t$ is related to the density $\lambda_t$ by $\Lambda_t = \mathrm{Z}\,\lambda_t$. In addition, $\lambda_t$ can be assumed to be an increasing function of the applied stress in the form of a power law function of the maximum principal stress $\sigma_1$:

$$\lambda_t = \lambda_0 \left[\frac{\langle\sigma_1\rangle}{S_0}\right]^m, \quad (3)$$

where $m$ and $S_0^m/\lambda_0$ are called the Weibull parameters (with $m$ the Weibull modulus and $S_0^m/\lambda_0$ the Weibull scale parameter). By using the weakest link hypothesis, the failure probability $P_F$ is the probability of finding at least one defect within $\Omega$ when ($\sigma_F=\sigma_1 > 0$).

$$P_F = P(\delta \geq 1, \Omega) = 1 - exp(-Z\lambda_0 \left[\frac{\sigma_F}{S_0}\right]^m) \quad (4)$$

In the case where the volume is loaded by a non-uniform field of stresses, the volume size is replaced by the effective volume as introduced by Davies (1973)

$$P_F = 1 - exp(-Z_{eff}\lambda_0 \left[\frac{\sigma_{max}}{S_0}\right]^m) \quad , \quad (5)$$

where $\sigma_{max}$ denotes the maximum value of the maximum principal stress in $\Omega$ the effective volume introduced by Davies (1973):

$$Z_{eff} = \int_\Omega \left(\frac{\langle\sigma_1\rangle}{\sigma_F}\right)^m dZ \quad \text{when} \quad \sigma_F > 0 \ , \quad (6)$$

One way to obtain these parameters is to deduce the Weibull modulus from the ratio of the standard deviation of failure stresses ($\sigma_{sd}$) to the average failure stress ($\sigma_w$) and the Weibull scale parameter ($S_0^m/\lambda_0$) from the average failure stress (Forquin and Hild, 2010):

$$\frac{\sigma_{sd}}{\sigma_w} = \frac{\sqrt{\Gamma\left(1+\frac{2}{m}\right) - \Gamma^2\left(1+\frac{1}{m}\right)}}{\Gamma\left(1+\frac{1}{m}\right)}, \quad (7)$$

$$\sigma_w = S_0(\lambda_0 Z_{eff})^{-1/m}\Gamma\left(1+\frac{1}{m}\right), \quad (8)$$

where $\Gamma$ is the Euler function of the second kind (Spanier and Oldham, 1987):

$$\Gamma(1+x) = \int_0^\infty exp(-u)u^x du \quad (9)$$

The coefficient of variation ($\sigma_{sd}$ / $\sigma_w$) is bounded by the functions (1/$m$) and ($\pi/\sqrt{6}m$). Therefore, the Weibull modulus gives a direct indication on the scatter in failure stresses, namely, the higher the Weibull modulus, the lower the standard deviation and the scatter of failure stresses with respect to the average value. A classical alternative to Eq. (7) for determining the Weibull modulus is to resort to the so-called Weibull (1939) diagram in which $ln[-ln(1-P_F)]$ vs. $ln(\sigma_F)$ is interpolated by a linear function, the slope of which is the Weibull modulus $m$.

Regarding the Weibull scale parameter, it can be deduced by inverting equation (8). In practice, this Weibull scale parameter doesn't need to be calculated since the mean failure strength of domain $\sigma_w^2$ characterised by an effective volume $Z_{eff}^2$ can be deduced from the following equation:

$$\sigma_w^2 = \sigma_w \left[\frac{Z_{eff}^2}{Z_{eff}}\right]^{-1/m}, \quad (10)$$

The Weibull modulus $m$ being positive, it is deduced from Equation (10) that the larger the effective volume $Z_{eff}^2$ of domain $\Omega_2$ the lower its strength. Conversely, the smaller the effective volume $Z_{eff}^2$, the higher its strength. This is the so-called scale (or size) effect predicted by the Weibull model.

## 4.3 Brittle materials: highly sensitive materials to pressure and strain-rate

For the last three decades the quasi-static confined strength of brittle materials has been extensively studied under various loading path and over a large range of loading-rates. In addition to standard tensile tests, diametral compression tests (Brazilian tests), uniaxial compression tests, triaxial compression tests were developed to provide an evaluation of the strength of materials (mainly rocks and concretes but also a few ceramics) under different confinement pressures. In these tests, a purely hydrostatic pressure is first applied to a cylindrical specimen. Afterwards, an axial compression is added. The deviatoric stress, which corresponds to the Mises stress in the present case, is taken as the maximum axial stress on withdrawal of the pressure applied by the confinement fluid. These tests have been carried out for several decades on rocks (Hoek and Franklin, 1968) (limestone and quartzite), concretes (Palaniswamy and Shah, 1974), and ceramics (Heard and Cline, 1980) (alumina-type ceramics, aluminium nitride, and beryllium or magnesium oxide). It is observed that these materials known for their brittle or quasi-brittle responses under tensile or uniaxial compression loadings undergo a change to a more ductile response under high confining pressure along with an increase of strength with pressures that may exceed ten times those under unconfined or nearly unconfined loading.

As spectacular as is the increase of strength and ductility with confining pressure, the increase in strength of unconfined brittle materials with strain-rate in both tension and uniaxial compression cannot be neglected above a certain threshold of strain-rate. For example, the peak stress sensitivity of ordinary or high-strength concretes to strain-rate when subjected to quasi-static and dynamic uniaxial compression has been investigated extensively during the three last decades. A synthesis proposed by Bischoff and Perry (1991) (Fig. 4.4) shows that, above a strain rate of $10^{-5}$ $s^{-1}$, a smooth and linear increase of strength with strain rate (in a log-log plot) is noted up to 20-30 $s^{-1}$. This effect is generally attributed to free water within the concrete sample since this phenomenon seems to be less observed in dry samples (Gary et al., 1991). Rossi (1988) observed a significant influence of free water on the toughness of concrete. Thus, the strain rate sensitivity of concrete below 20-30 $s^{-1}$ could result from the viscosity of free water that impedes the opening of micro-cracks (Rossi, 1991).

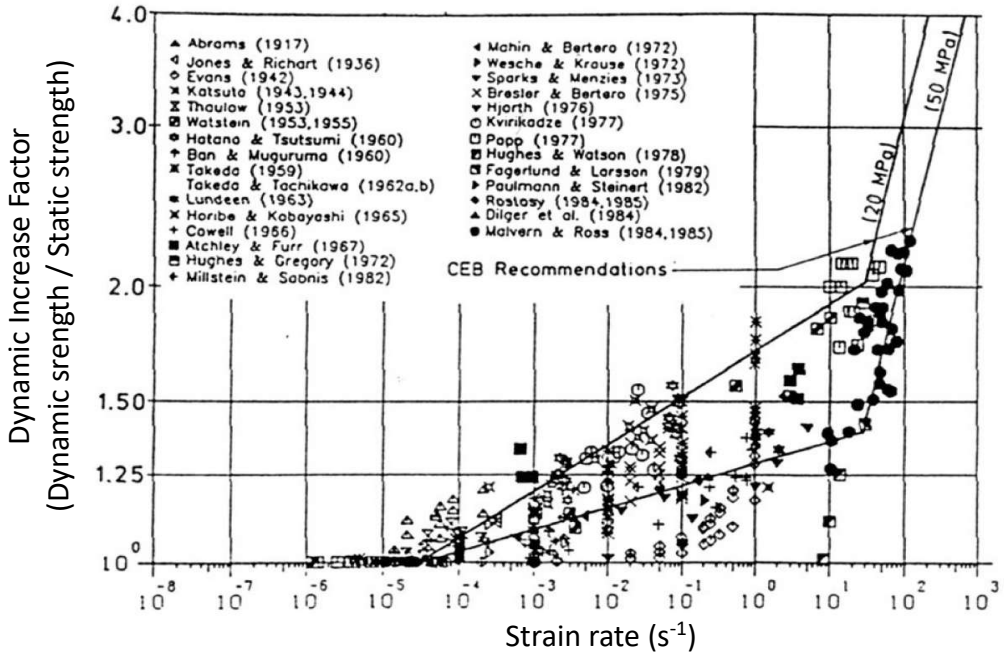


Figure 4.4 - Influence of strain-rate on the strength of concrete in uniaxial compression tests according to the review of proposed by Bischoff and Perry (1991)

Above 20-30 $s^{-1}$, the increase of strength in concretes in dynamic uniaxial compression is more pronounced. Free water cannot the main reason for the phenomenon since it is also observed in dry concretes (Gary et al., 1991). According to Gorham (1989) and Weerheijm (1992), this increase of ultimate stress is, at least in a large part, the consequence of inertial effects that restrain the lateral expansion associated with compression. Indeed, due to inertial forces acting as an artificial confinement and due to the sensitivity of brittle materials to confining pressure, it could explain the apparent strain-rate sensitivity that is observed in concrete-like materials in dynamic unconfined loading conditions. This interpretation is also supported by the strongly reduced strain-rate sensitivity of concrete and rock materials when subjected to dynamic quasi-oedometric (meaning quasi-uniaxial-strain) compression (QOC) tests for which the radial displacement is considerably reduced (Forquin, 2003; Forquin et al., 2008a). In QOC tests a cylindrical sample is placed within a (metallic) confining cell. The gap between the sample and the ring is totally filled with a polymeric resin that hardens in less than 24 hours. Next, the sample is axially compressed and the strength is deduced from the axial stress on withdrawal of the radial

stress deduced from a strain gauge taped to the outer surface of the ring. The static response of various types of concrete is compared to the dynamic response in (Forquin et al, 2010; Forquin, 2015; Piotrowska and Forquin, 2015) showing that even if the influence of the loading-rate cannot be neglected it remains much weaker than in the absence of confinement.

As discussed above, the increase of ultimate strength in concrete under dynamic uniaxial compression is generally attributed to free water in the material (below 20-30 $s^{-1}$) or inertial effects (above 20-30 $s^{-1}$). However, strain-rate sensitivity of brittle materials is also observed in dynamic tensile loadings for which no inertial confinement occurs. A synthesis of results obtained with concretes was proposed by Klepaczko and Brara (2001). As in uniaxial compression, a low increase of strength with loading rate is observed up to about 1 $s^{-1}$. Above this transition, a sharp increase of strength is reported. Free water within concrete specimen may explain the sensitivity at low strain rates. Toutlemonde (1994) performed direct tensile tests for strain rates in the range of ($2.5\times10^{-6}$ $s^{-1}$ - 2.5 $s^{-1}$). Significant strain-rate sensitivity was observed in wet concretes for a maximum aggregate size ranging from 2 to 10 mm, and for water to cement ratios varying from 0.3 to 0.7. Conversely, a more limited influence of loading rate was detected in dry specimens. Spall tests performed by Forquin and Erzar (2010) on a dried or water-saturated micro-concrete revealed a spectacular increase of dynamic tensile strength in the strain-rate range of (20 $s^{-1}$ – 120 $s^{-1}$) (Fig. 4.5a). Similar results for the "Dynamic Increase Factor" (i.e., ratio between the dynamic and quasi-static strengths) were obtained in the strain-rate range of (10–100 $s^{-1}$) by Weerheijm (1992), Wu et al. (2005) and Schuler et al. (2006) on ordinary and high-strength concretes. A post-mortem analysis of several samples after spalling tests was conducted by Forquin and Erzar (2010) and Erzar and Forquin (2011). These tests revealed an increase of cracking density with strain-rate along with a pronounced effect of free-water content, the amount of visible cracking being much more pronounced in dry concrete and microconcrete than in their wet counterparts. This observation is consistent with observations made in EOI (edge-on-impact) tests presented in the next subsection.

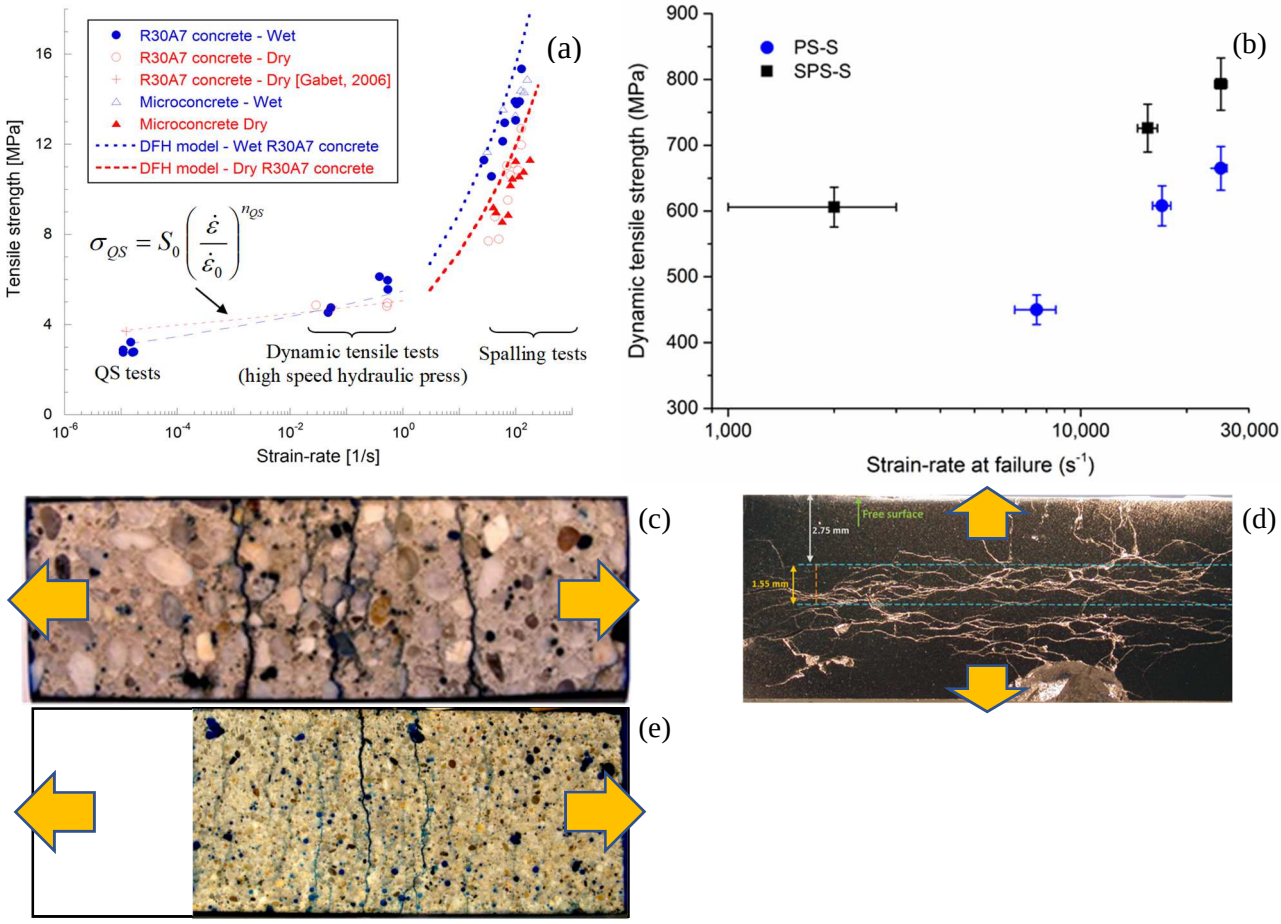


Figure 4.5 - Influence of strain-rate on the tensile strength of brittle solids (Forquin et al, 2021). (a) Case of dry and wet microconcrete and common concrete (Erzar and Forquin, 2014; Weerheijm and Forquin, 2013), (b) Case of two SiC ceramics (Zinszner et al, 2017), (c) Post-mortem analysis of dry common concrete after a spalling test at 120 $s^{-1}$ (Erzar and Forquin, 2011), (d) Microscopic view of the SPS-S damaged specimen recovered after a test performed at 2,000 $s^{-1}$ (Zinszner et al, 2017), (e) Post-mortem analysis of dry microconcrete after a spalling test at 130 $s^{-1}$ (Forquin and Erzar, 2010).

Recent studies performed with ceramics have shown the strong strain-rate sensitivity of their tensile strength. For instance, high-pulsed power generator (GEPI) equipment was used to perform spall tests on alumina (Zinszner et al, 2015) and SiC ceramics (Zinszner et al, 2017) at controlled strain rates. The GEPI technique consists in transferring an intense pulsed current to a loop-shaped conductive electrode to generate a tailored ramp pressure via the Laplace effect. This pressure is transferred to the ceramic sample put in contact with the electrode. Therefore, a rise time of about 0.2–0.5 µs can be

reached and the strain rate levels in the specimen are in the order of $10^4$-$10^5$ $s^{-1}$. The dynamic strength of 2 silicon carbides as a function of the applied strain-rate is depicted in Fig. 4.4b. A clear increase of strength with strain-rate is noted with both SiC microstructures. Similar results were more recently obtained with shockless plate-impact spalling tests conducted with new geometries of wavy-machined flyer plates (Dargaud and Forquin, 2021).

To summarize, although brittle materials often remain "repellent" materials in the field of engineering mechanics, it can be observed that these materials show much more attractive properties under extreme conditions such as high temperatures, high pressures or high loading rates. In particular, under confinement the brittle response can give way to ductile behaviour characterised by strain or pressure hardening. In addition, as it will be explained in the following subsection, above a certain loading rate, the well-known brittle and probabilistic behaviour of these materials under tensile loading may change into a deterministic behaviour characterized by an increase of ultimate failure stress and strain with loading rate. Moreover, the ubiquitous weakest link hypothesis no longer applies and the failure is not controlled by a unique initiation site but is the consequence of a large number of oriented cracks.

## 4.4 Damage and deformation modes involved in brittle materials under high-strain rate loadings

As discussed in the previous subsection, brittle materials display mechanical responses under high rate loading that strongly differ from their response under static loading. Indeed, most of them exhibit a strong sensitivity to strain-rate contrary to their static behaviour. In addition, as it will be explained in the following subsection, the probabilistic and size-dependent behaviour gives way to a deterministic behaviour with a much less influence of size. Given the role played by microstructural parameters (flaws, heterogeneities, interfaces…) and the nature of mechanisms at the microscopic scale it is of major importance to better understand and characterise these mechanisms and to develop, when possible, micromechanics-based models enabling the bridging of microstructural parameters and the microcracking mechanisms with the macroscopic behaviour.

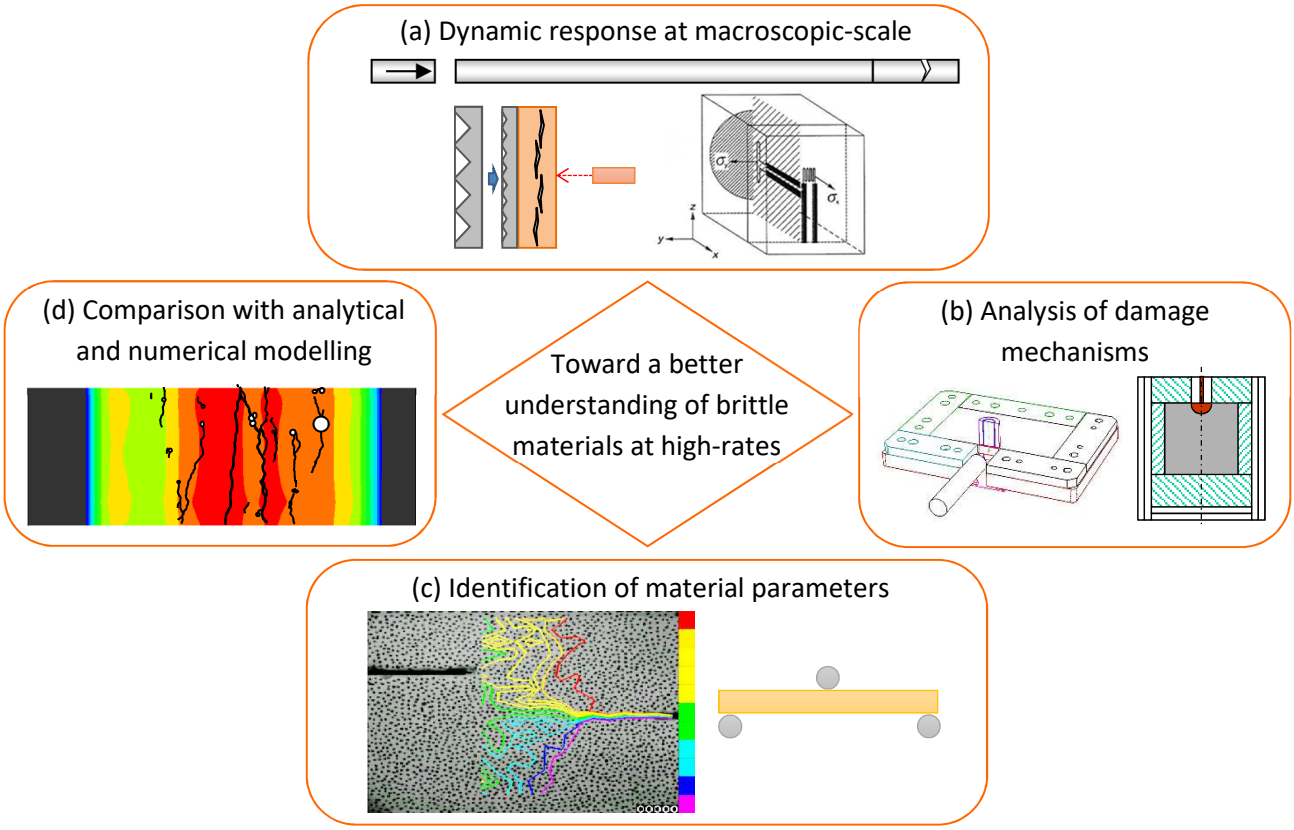


Figure 4.6 - Use of different testing methods for the development of a micromechanics-based model. (a) Techniques to characterize the dynamic response at the macroscopic scale; among them those using Hopkinson Pressure Bar apparatus and plate-impact facilities. (b) Techniques to characterize the damage mechanisms in brittle materials; among them the edge-on impact testing technique with ultra-high-speed imaging and post-mortem observation. (c) Techniques to identify specific model parameters; among them the rocking spalling test to characterize the crack speed in concrete (Forquin, 2012). (d) Techniques to validate the constitutive model based on comparison at macroscopic and microscopic scales. The spalling technique can be used for this purpose. (Figure derived from (Forquin, 2017; 2021)).

To do so, the strategy depicted in Fig. 4.6 can be considered. Damage mechanisms at a microscale can be analysed, for instance, by time-resolved observations made with ultra-high-speed imaging (Forquin and Hild, 2008), synchrotron radioscopy (Lukic et al, 2022) or full field measurements (Forquin and Lukic, 2016) along with post-mortem studies (measurements of cracking densities as performed by Duplan and Forquin (2021)) (Fig. 4.6a). It also requires parameters adjustment regarding the population of defects activated at high stress-rate as was reported by Forquin et al. (2021) and regarding the crack speed as achieved through the rocking spalling technique (Forquin, 2012) (Fig. 4.6b). Next step, focus on model validation that can be performed through a comparison between numerical predictions and experimental observations at a microscopic scale (Fig. 4.6c) and at a macroscopic scale (Fig. 4.6d). In the next subsection some experiments performed for exploring the damage mechanisms induced in brittle materials at high-rates are presented.

### 4.4.1 Investigation of tensile damage in ceramics by means of Edge-On-Impact tests

The edge-on impact (EOI) testing technique constitutes one of the most efficient and easiest experimental methods to investigate and to visualize the growth of tensile damage induced in brittle solids when subjected to high-strain rates. This method was pioneered by Strassburger and coworkers in EMI (Ernst-Mach-Institut) (Senf et al., 1994; Strassburger, 2004) and by Riou and coworkers in CTA (Centre Technique d'Arcueil, DGA) (Riou et al. 1998; Denoual and Hild 2000; Forquin et al. 2003). It consists in the impact of a cylindrical projectile against one of the edges of the tested ceramic tile. The projectile is usually larger in diameter than the target thickness and much smaller than the target height. It results in an impulsive loading characterized by a very short rise time (less than 1 µs). The loading, of triaxial shape in the vicinity of the contact area, turns into a bi-dimensional (plane stress) divergent wave propagating in the whole target. It is the reason why the stress amplitude is expected to decline more slowly (as $1/\sqrt{r}$) compared to a spherical expansion for which a decrease (as $1/r$) is observed. Accordingly, damage develops much further in distance which facilitates the observations with a high-speed imaging system. In the so-called open-configuration, the lateral face of the target is visualized with an ultra-high-speed camera set at frame-rates from 2 µs down to 0.1 µs. The camera can be installed along the axis of the reflection of the incident light provided by a flash or continuous light unit. The visualized surface is usually polished to increase the amount of light captured by the camera but also to improve the observation of cracks by contrast. This experimental method provides several advantages compared to other testing techniques. In particular, much higher strain-rates can be achieved than in techniques requiring a correct mechanical balance of the sample such as Brazilian tests performed with SHPB apparatus. For instance, in EOI tests conducted by Forquin et al. (2018), typical strain-rates ranging from a few thousands of $s^{-1}$ to a few tens of thousands of $s^{-1}$ were generated, leading to an intense multiple fragmentation process in the targets.

In contrast, the spalling test method by plate-impact or by pulsed-power technology provides the advantage of a direct measurement of the spall strength and provides much higher strain-rates (mostly above $10^4$ $s^{-1}$). However, the spall fracture is hidden within the bulk of the sample and so cannot be visualized by high-speed photography. In addition, the fracture pattern remains difficult to analyze through post-mortem observations. The edge-on impact testing technique also requires a much less costly gas gun facility compared to those used for plate-impact tests, which operate with a larger caliber and under vacuum, or compared to pulsed power generator facilities.

In the experiments performed by Riou et al. (1998) a hard-steel cylinder projectile (D11H20) impacted the edge of a dense natural sintered Silicon Carbide at an impact velocity ranging from 100 to 300 m/s. In some of the experiments, the ceramic tile was backed with a steel confinement beam (see Fig. 4.7a). The ceramic beam dimensions are 100 mm x 10 mm x T where the thickness T is equal to 15 or 20 mm. Two pictures taken 2.9 µs after impact with an Imacon 790 high-speed camera are shown in Figures 4.7b and 4.7c. The first picture (Fig. 4.7b) corresponds to a SiC beam tested without steel backing at an impact velocity of 250 m/s. In the second test (Fig. 4.7c), the SiC target is constrained on its back by a steel beam and is impacted at close to the same impact speed (260 m/s). A damage pattern composed of a large number of oriented short cracks is observed in less than 3 µs. It is concluded by the authors that the backing-steel confinement does not change the initial damage shape generated in the first 3 µs whereas the presence of the confinement limits the initiation of transverse (spall) cracks in the following two µs.

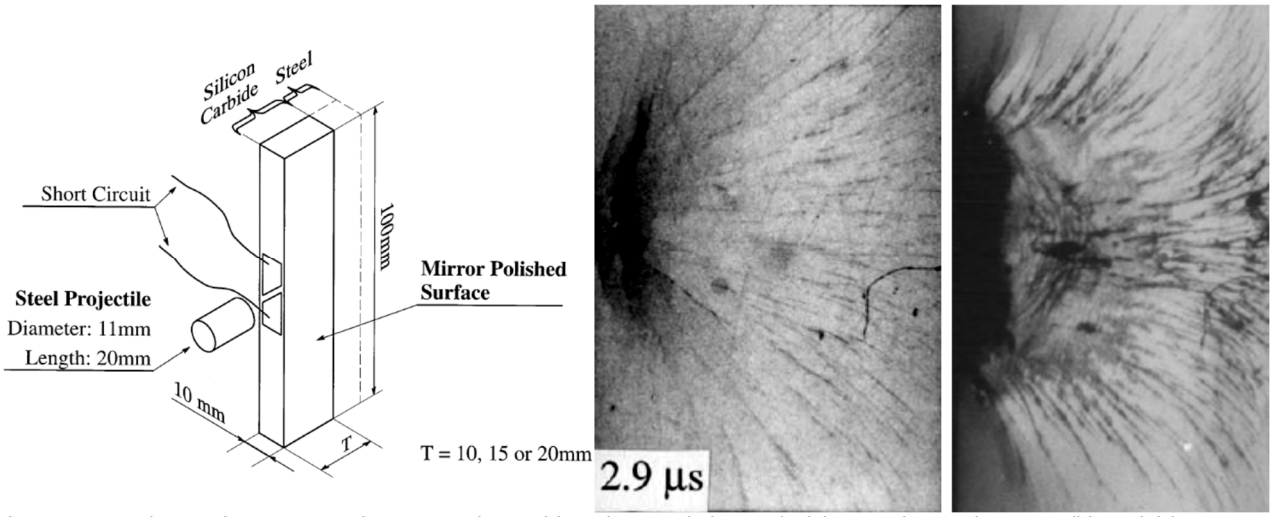


Figure 4.7 - Edge-on impact experiments performed by Riou et al. (1998a). (a) Experimental set-up, (b) and (c) Damage at 2.9 µs, (b) Unconfined 15 mm thick SiC target impacted at 250 m/s, (c) Backing steel confined 15 mm thick SiC target impacted at 260 m/s.

The fragmentation process induced in a porous SiC ceramic and in the same ceramic that is filled with an aluminum alloy through its open porosity was investigated by Forquin et al. (2003) by means of EOI tests in an open configuration (using a high-speed camera) and also in a sarcophagus configuration. This second configuration is depicted in Fig. 4.8a. It is composed of a metallic casing made of an aluminum alloy that surrounds the ceramic tile with the aim of keeping the fragments in place. Small paper wedges are placed in-between the ceramic tile and the aluminum casing to ensure an impedance discontinuity. It is the reason why the same number of cracks are expected for both configurations. After impact, the fragmented ceramic tiles were infiltrated in the sarcophagus with a hyper fluid resin (Epoxy, Struers) and then polished for optical observations as shown in Figures 4.8b, 4.8c and 4.8d. The tests conducted at 100 m/s and 200 m/s revealed an increase of the cracking density in R-SiC ceramic with an increase of loading-rate. The test performed at an impact speed of 200 m/s with the infiltrated ceramic showed a decrease of the intensity of fragmentation compared to the non-infiltrated ceramic and also a very good residual strength. The fragmentation process was simulated with a finite-element code implementing the DFH (Denoual-Forquin-Hild) anisotropic damage model along with Weibull parameters identified from bending tests. The experimental and numerical results demonstrated that the aluminum alloy infiltrated via the open porosity of the ceramic results in two beneficial effects: on the one hand it increases the crack-inception stress thereby lowering the cracking density. On the other hand, it creates a bridging effect leading to a much higher residual strength of the fragmented targets. Both effects are seen to be beneficial regarding a multi-hit loading scenario.

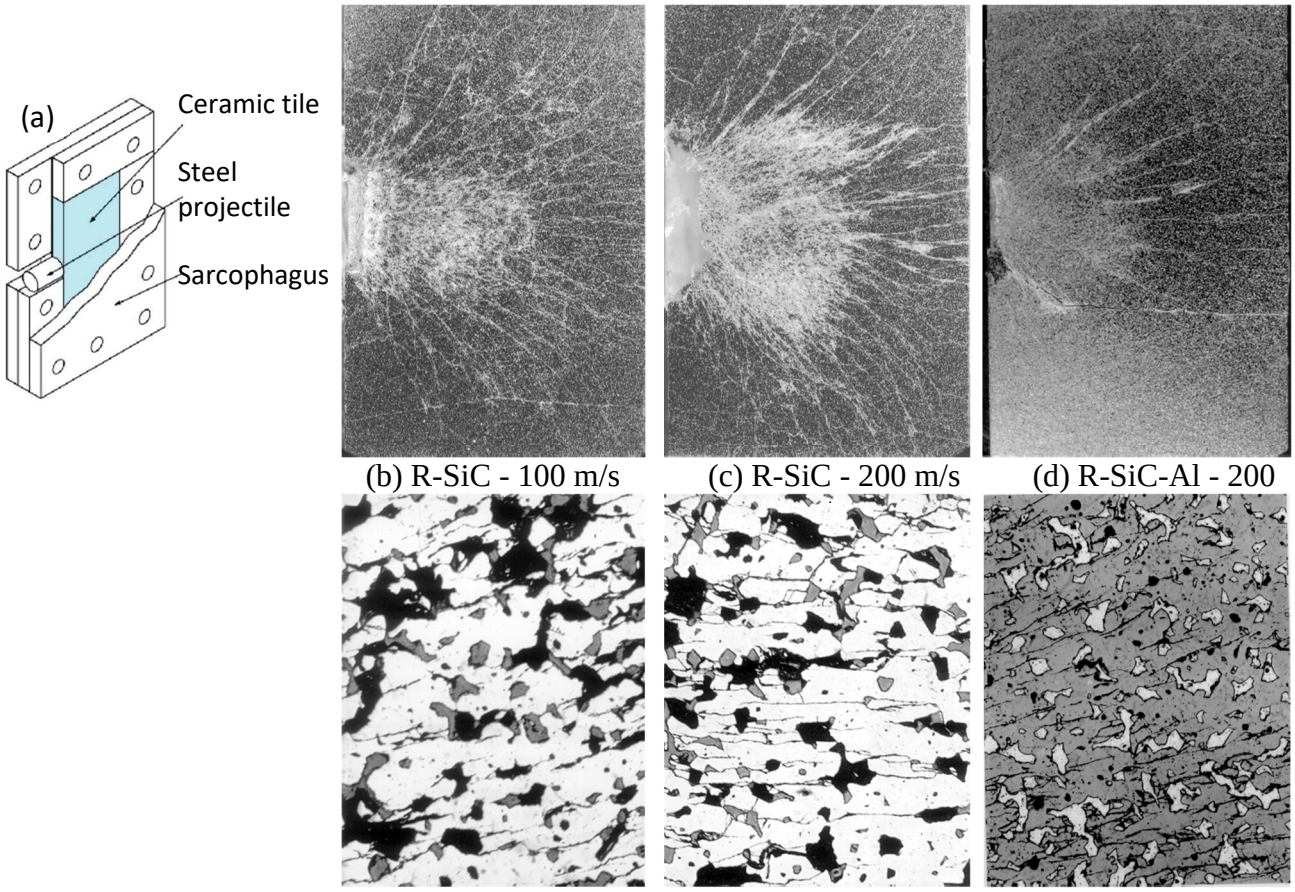


Figure 4.8 - Edge-on impact experiments performed by Forquin et al (2003). (a) Sarcophagus configuration, (b) R-SiC target impacted at 100 m/s, (c) R-SiC target impacted at 200 m/s, (d) R-SiC-Al target impacted at 200 m/s.

In the work developed by Riedel et al (2010), the elastic stress histories involved in an EOI test were numerically investigated and compared to those involved in a depth-of-penetration (DOP) test configuration and planar plate impact (PPI) experiments. In addition, the fracture processes in the target were numerically simulated with a mesh-free SPH code. It is concluded that an anisotropic damage representation along with tensile stress failure criteria are required to represent the damage propagation produced by diverging shock waves.

In the work conducted by Leavy et al (2013) the EOI technique is used as a benchmark to validate ceramic constitutive models implemented in a dynamic simulation code. To do so, a Weibull distribution is introduced in a hydrostatic tension criterion for describing the variability of material strength and the numerical predictions in terms of damage velocity versus impact velocity are compared to experimental observations provided by high speed photography. More recently, the edge-on impact techniques were extended to the investigation of the fracturing process in transparent armour ceramics such as single crystal (sapphire) and AlON (spinel) polycrystalline ceramics (McCauley et al. 2013). In the experiments performed by Forquin and Zinszner (2017) (Fig. 4.9), monocrystalline sapphire ceramic targets of size 60x60x4 $mm^3$ were subjected to the impact of a cylindrical projectile 10 mm in diameter at an impact speed of about 230 m/s. As illustrated by the pictures taken using a Kirana ultra-high-speed camera the fragmentation process develops within ten microseconds. It is observed that cracks propagate following specific orientations in relation to the C axis direction.

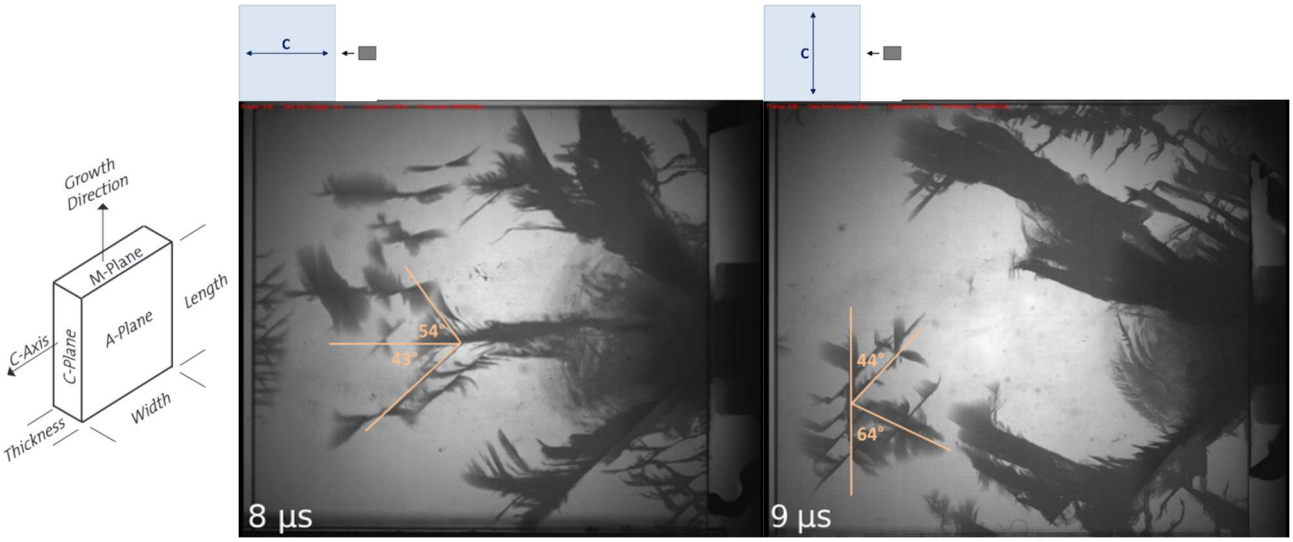


(a) (b) (c)

Figure 4.9 - Edge-on impact experiments performed against sapphire single crystal at an impact speed around 230 m/s (Forquin and Zinszner 2017). (a) Sapphire single crystal orientation (Saint-Gobain doc.). (b) Impact direction parallel to the C axis (horizontal axis). (c) Impact direction orthogonal to the C axis (vertical axis).

The intergranular and transgranular fracturing observed in polycrystalline AlON transparent ceramics subjected to EOI tests in McCauley et al. (2013) was numerically simulated by Zhang et al. (2018) using a peridynamics numerical method. For this purpose, a model in which individual grains are represented was built. This numerical approach allows both the description of the primary failure front that grows at intersonic (supershear) propagation speed as well as localized cracks which develop at sub-Rayleigh propagation speed.
The EOI experiments conducted on AlON by Strassburger (2004) were analyzed and modeled by Tonge and Ramesh, (2016) by considering a micromechanics-based model in order to describe the damage growth, the deviatoric and volumetric granular flow and pore compaction mechanisms that develop preferentially in the interior of the plate rather than on the surface due to inertial confinement. Again, the flaw distribution is observed to be an important parameter to account for the role of microstructure on the damage process.
In conclusion, the edge-on impact testing configuration has been used extensively for the last three decades to explore the fragmentation process in different kinds of ceramic armours. High-speed photography has revealed several features of the fragmentation process generated in these materials under impact loading. In particular, it is observed that the fragmentation process is composed of a large number of cracks oriented perpendicularly to the positive principal stress. A numerical investigation of the loading history is presented thereafter. Next, a comparison of the fragmentation properties of 4 SiC ceramics is proposed.

### 4.4.2 Investigation of tensile damage in concrete and rocks by means of edge-on-impact tests

The EOI testing technique with dynamic confinement system was applied to MB50 micro-concrete plates (200 x 120 x 15 $mm^3$) in Forquin and Erzar (2010) by using a cylindrical projectile 22.5 mm in diameter and 100 mm in length made of high-strength aluminum alloy. The projectile was projected onto the edge of the target at a speed of 50 m/s. In these experiments half-cylinders made of steel were used as dynamic confinement. The specimens were infiltrated post-mortem and polished to reveal the damage pattern. The results obtained on dry and wet specimens are reported in Fig. 4.10a. It can be seen that the cracking density is much higher in the dry specimen compared to the wet sample. Moreover, the cracks induced in the wet target seem to be much thinner. Finally, free water in the micro-concrete is seen to play a major role on the damage pattern. This is confirmed by spalling tests which show a lower tensile strength in dry MB50 microconcrete compared with wet MB50 microconcrete over the whole range of strain-rates explored (30-150 $s^{-1}$) (Forquin and Erzar, 2010). Edge-on impact experiments as well as spalling tests were also conducted on R30A7 concrete (max. aggregate size: 8 mm) to determine the influence of aggregate size (Erzar and Forquin, 2011). The damage patterns presented in Fig. 4.10b confirm the previous observations: the damage is much more pronounced in the dry tile compared to the wet specimen. In the same way as the dry MB50 micro-concrete, intense cracking developed near the impacted area. In addition, many long radial cracks are observed in the dry R30A7 plate. By contrast, the cracking network is less developed in the wet tile: several cracks are present but their opening is limited. Besides, one can see that few aggregates are broken: cracks have circumvented the inclusions during their propagation. Again, this result is seen to be consistent with spalling experiments which exhibited a much higher strength with wet samples than with dry samples (Erzar and Forquin, 2011; 2014). It is the reason why the water content needs to be taken into account in numerical modelling to be used for numerically simulaing ballistic impact against a concrete target.

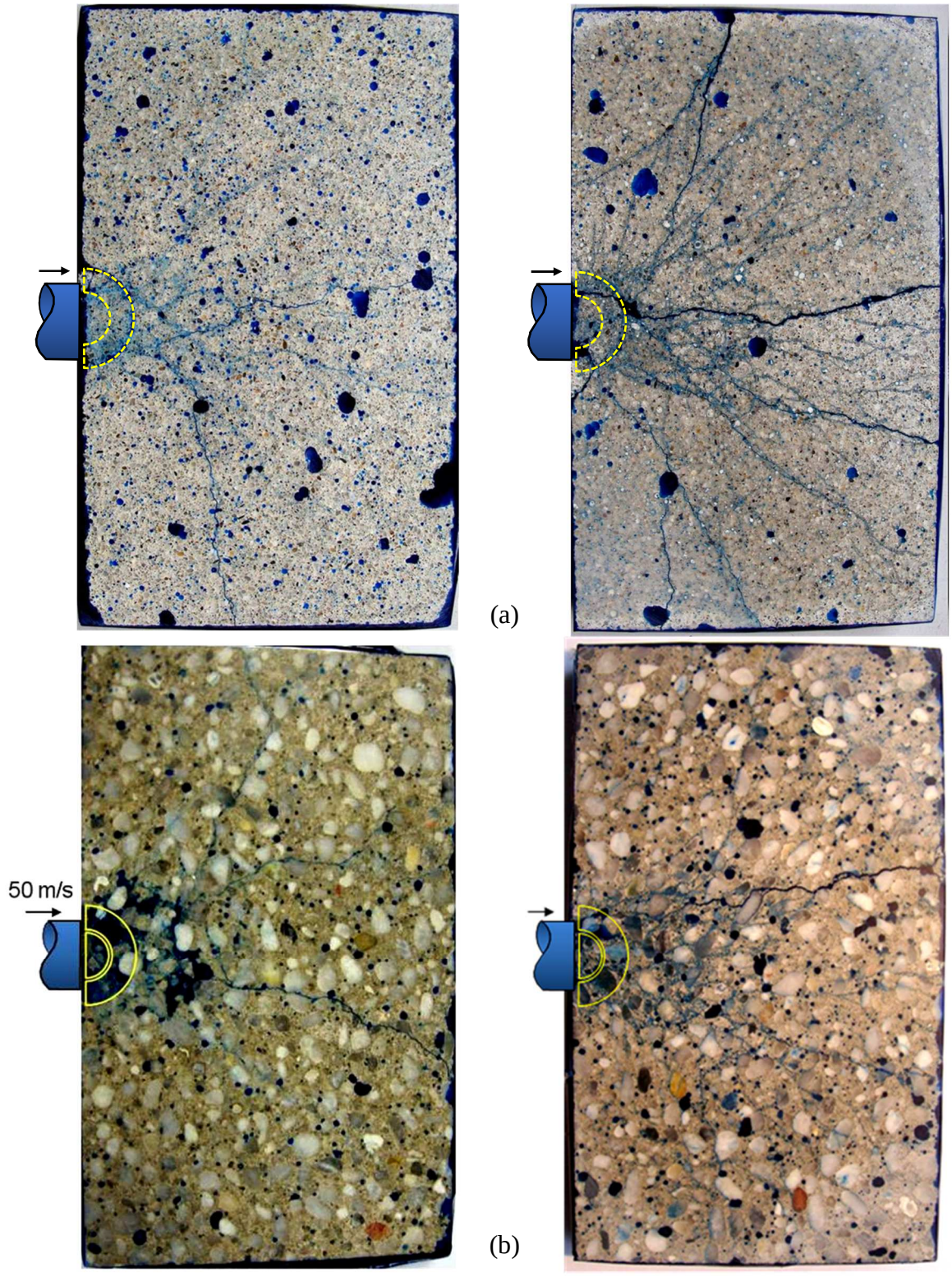


Figure 4.10 - EOI test conducted with dynamic confinement in sarcophagus configuration at striking velocity: 50 m/s. (a) MB50 microconcrete (Forquin and Erzar, 2010), (b) R30A7 concrete (Erzar and Forquin, 2011) tested in wet condition (left) and dry condition (right).

### 4.4.3 Investigation of mode II fracturing modes in ultra-high performance concrete by means of edge-on-impact tests

In the example of Fig. 4.11, fiber-reinforced Ductal® concrete tiles are subjected to the EOI test with a steel projectile and a striking velocity of about 130 m/s. The first EOI test (Fig. 4.11a) was conducted in open configuration in which an ultra-high speed camera is used to visualize the development of the fragmentation process. Compressive damage composed

of involute (curved) cracks develops in less than 20 µs after impact. Then, the damage zone darkens due to the tilt of the visualized surface. Furthermore, 44 µs after impact, multiple straight radial cracks appear due to tensile hoop stresses. Spall cracks, oriented perpendicularly to the projectile axis, are observed 44 µs after impact 70 mm from the impact point. The distance between spall cracks and the rear edge (60 mm) corresponds approximately to the projectile length (50 mm). The time to initiation is consistent with a wave velocity close to 5000 m/s (38 µs are required to travel 190 mm).

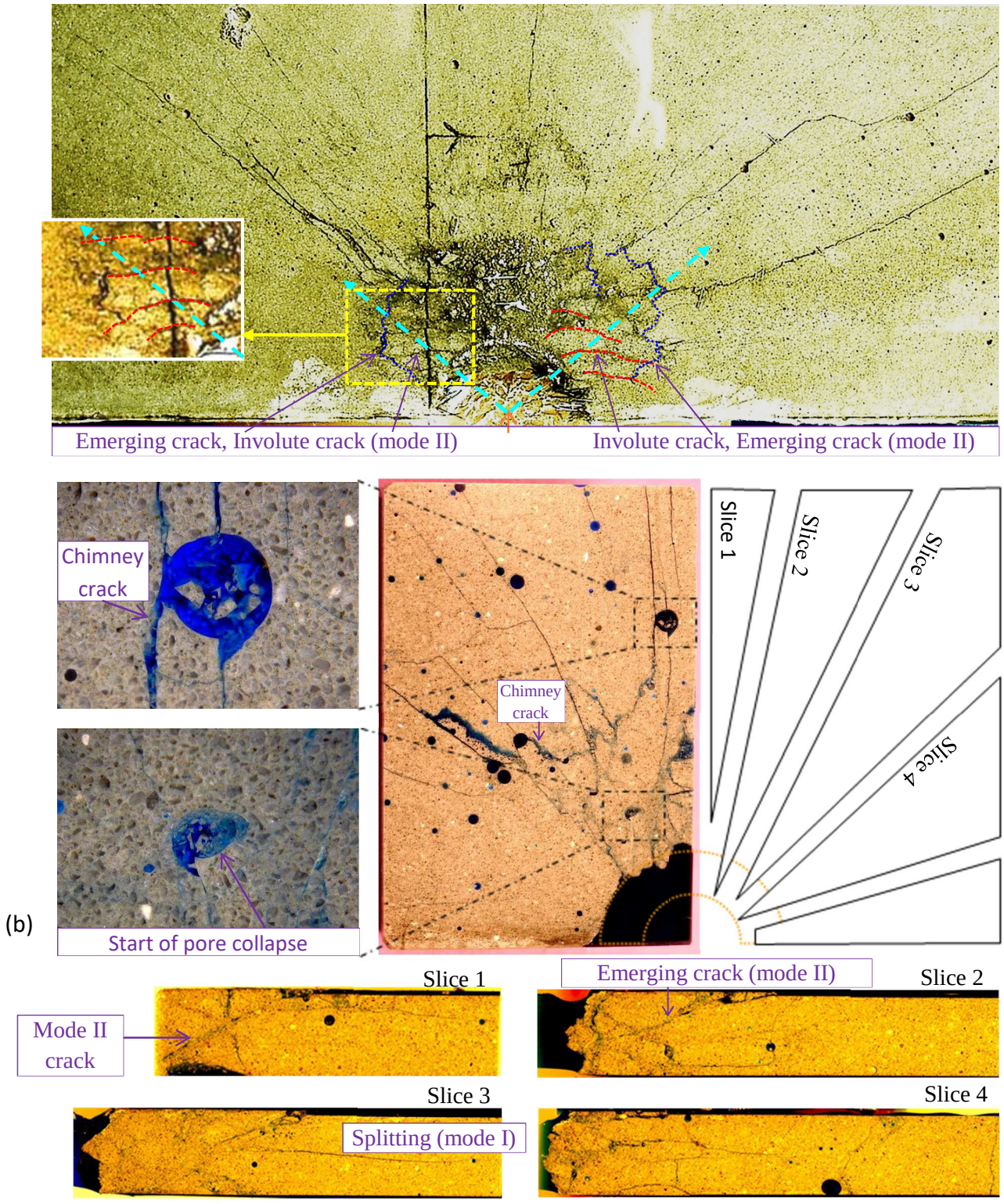


Figure 4.11 - EOI test conducted with steel projectile and dynamic confinement system with Ductal® concrete without fiber. (a) Open configuration, striking velocity: 130 m/s. (b) Sarcophagus configuration, striking velocity: 130 m/s (Forquin, 2003).

The final damage pattern is more easily analyzed with the sarcophagus configuration (Fig. 4.11b) and several damage modes are observed as a function of the distance from the impact point:

- Close to the impact point the confined zone is totally damaged and reduced in debris despite the fibers that reinforce the target,
- Beyond the confined area involute cracks (also called snail cracks) are observed. It can be noted that these cracks are more or less oriented at 45° with respect to the radial and hoop directions and correspond to mode II cracks with rubbing lips,
- Moreover, circular-front cracks are centered on the impact point. These cracks are thought to emerge onto the surface leading to the dark areas observed in pictures taken by the ultra-high speed camera between 16 µs and 44 µs after impact. These “emerging cracks” or “shell cracks” are supposed to result from unconfined compression beyond the confined area,
- This confined damage does not prevent intense fragmentation of the tile at a distance of 40 mm to 130 mm from the impact point. This fragmentation is composed of numerous radial cracks, which are a few centimeters long,

Finally, Figure 4.11b well illustrates the typical damage modes involved in brittle materials under confining pressure and dynamic tensile loading. Whereas mode II (shearing) fracturing and pore collapse processes may occur under confinement, multiple fragmentation is observed in dynamic tension.

### 4.4.4 Investigation of microplasticity and micro-cracking modes in ceramics by means of pyrotechnic spherical expansion test

The pyrotechnic spherical expansion test consists of detonating a half-sphere of explosive in a medium known to be semi-infinite (Fig. 4.12a). The loading shows some similarities to one generated by projectile impact. Nevertheless, it provides the following advantages: this loading is limited in time, the material does not undergo the phase of penetration of the projectile which erodes and destroys the pattern of damage. In addition, the compression is almost perfectly spherical, unlike an impact which remains dependent on the projectile/target contact conditions and which leads to a more heterogeneous stress field. However, the levels of pressure and strain rates is related to the nature of the explosive used but can be estimated thanks to a numerical simulation of the test. This calculation can be readjusted by comparing some numerical predictions to the experimental data provided from laser interferometry or pressure gauge measurements.

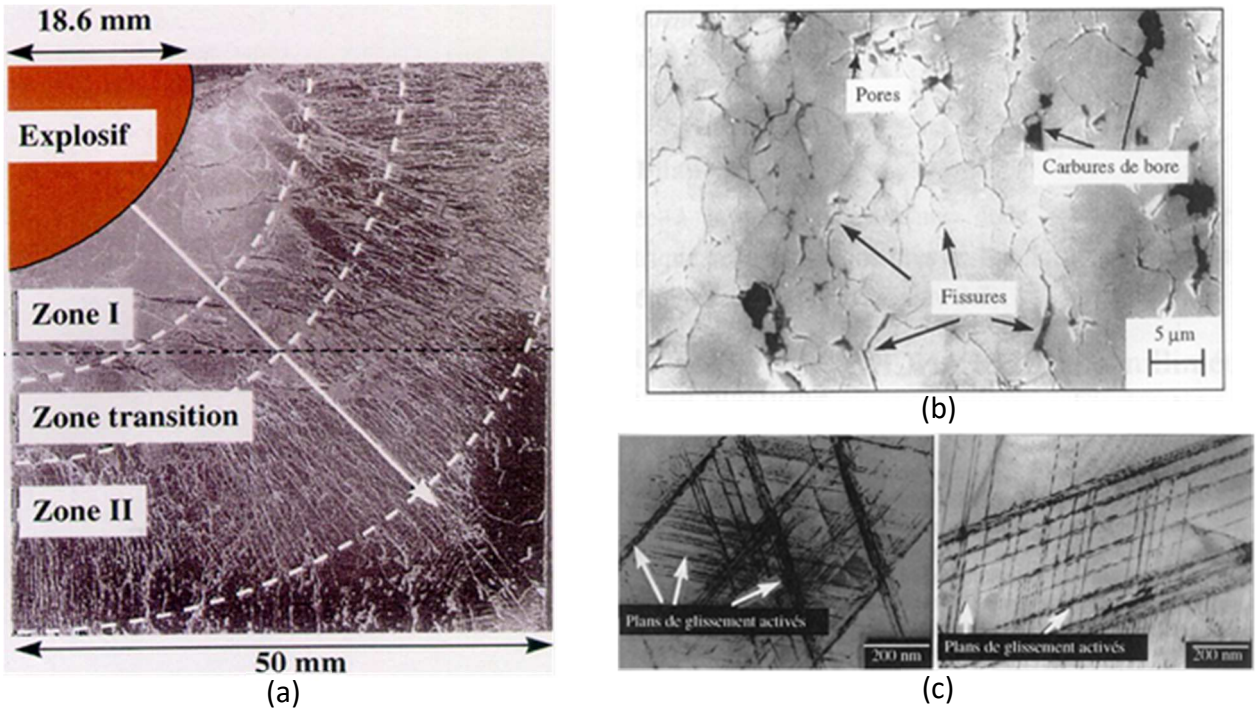


Figure 4.12 - Pyrotechnic spherical expansion tests performed on a silicon carbide (S-SiC grade) ceramic. (a) Zones of damage and a transition zone, (b) cracks and damage of the first zone, and (c) close-up of activated slip planes in the grains.

The pyrotechnic spherical expansion technique was first developed by Larson (1982) and implemented on alumina ceramics by Cagnoux (1990) and Cosculluela (1992). This technique was used more recently by Malaise (1999) on silicon carbide (S-SiC grade). A post-mortem study shows two distinct zones of damage and a transition zone (Fig. 4.12a). The first zone extended over 10 mm is characterized by intense damage consisting of cracks a priori without particular orientation (Fig. 4.12b). This cracking is probably initiated from activated slip planes in the grains (Fig. 4.12c). The second zone located more than 17 mm from the explosive shows intense cracking oriented in the radial direction characterized by

millimeter-sized cracks. This multiple cracking of the ceramic, subsequently called fragmentation, was created by the tensile hoop-stresses. The compression loading preceding that of tension, the isotropic damage created in the zone I prevented this anisotropic damage visible in the zone II occurring in the zone I.

In Cosculluela's PhD thesis (1992), this technique was applied to two alumina grades, one coarse-grained and one fine-grained. Again, a hemispherical cavity machined at the top of each block was used to place the explosive so a divergent spherical wave was generated in each block. TEM microscopy observations were performed considering thin-sections picked up from three abscissas.

*TEM observations for coarse-grained alumina (Cosculluela and Forquin, 2021)*

- r = 25 mm (Fig. 4.13a): Very close to the explosive, microplastic phenomena are very numerous (twins, dislocations). The picture also shows a network of intergranular microcracks. The micrographs show residues of a glassy phase at the grain boundaries,. Otherwise, it seems that the microcracks appear preferentially near the most microplasticized grains.
- r = 45 mm (Fig. 4.13b): Microplastic activity is much less important. It is reduced to a few dislocation movements observed on part of the grains (approximately 50%). The picture shows the presence of transgranular microcracks. But this phenomenon is not representative of all the observations performed (Cosculluela, 1992). Some rare intergranular microcracks are observed.
- r = 58 mm (Fig. 4.13c): Microplastic activity is relatively a little less to what has been observed for the previous abscissa. The micrograph exhibits an intergranular microcrack.

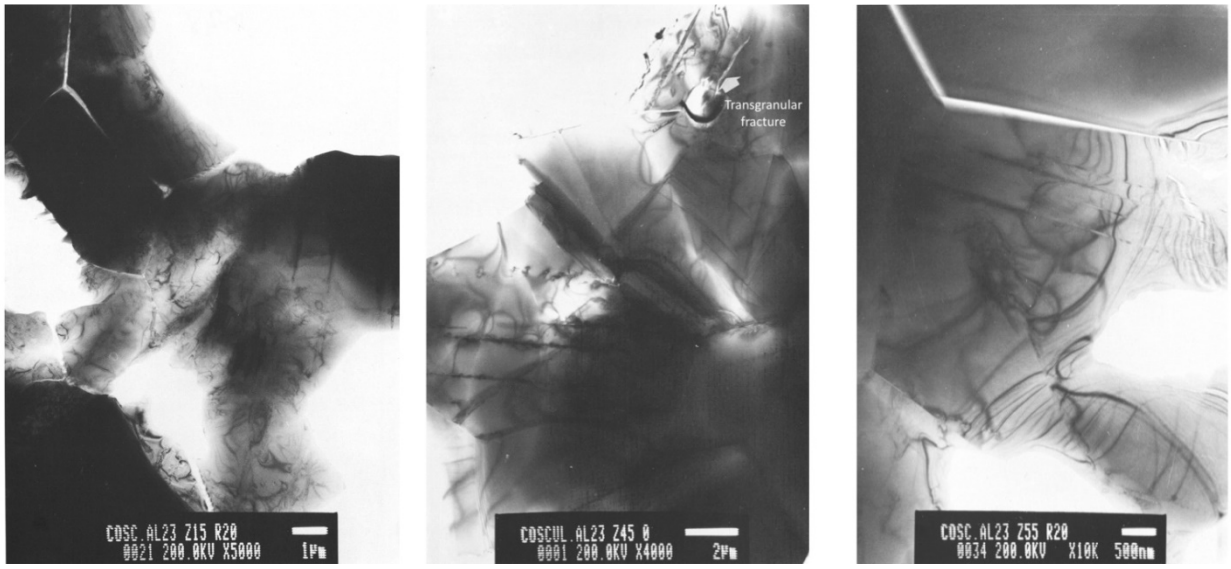


(a) (b) (c)

Figure 4.13 - TEM observations of coarse-grained alumina recovered after a divergent spherical wave behaviour test. (a) *r* = 25 mm, (b) *r* = 45 mm, the arrow shows a transgranular microcrack from a pore and not connected with the grain seal, (c) *r* = 58 mm.

*TEM observations for fine-grained alumina (Cosculluela and Forquin, 2021)*

- r = 20 mm (Fig. 4.14a): Near the explosive, the microplasticity activity is very important. Most of the grains exhibit dislocations and twins. Micrographs show an important network of intergranular microcracks (white lines). Additional observations made it possible to find that this network is dense and not oriented. The density of microcracks is not more prominent in the most microplasticized areas. These microcracks seem to be wider when they are next to the larger grains.
- r = 30 mm (Fig. 4.14b): Microplasticity activity is still very important. Alumina is the seat of the same physical phenomena than at the previous abscissa with a decrease in the densities of microcracks and twins. However, the relationship between microplasticity and microcracking remains difficult to establish.
- r = 50 mm (Fig. 4.14c): The observations made at this abscissa show the absence of intergranular microcracks. Microplasticity activity has almost disappeared even if a few dislocation stacks are still observed.

In conclusion, TEM observations performed at different locations in targets made of coarse-grained alumina, fine-grained alumina and SiC ceramic and subjected to pyrotechnic spherical expansion demonstrated that, in the area where stresses exceed the HEL (Hugoniot Elastic Limit) microplasticity activity consisting in dislocations, twins or activated slip planes in the grains along with intergranular or transgranular microcrack network are observed. However, the relationship between microplasticity and microcracking still needs to be established. Beyond a transition zone, as the level of radial stresses decreases, the isotropic damage created in the zone I leaves room for an anisotropic damage visible in the zone II. Thus,

the pyrotechnic spherical expansion technique appears as a powerful testing technique to analyze and characterize the damage and deformation processes in brittle materials caused by a divergent spherical wave.

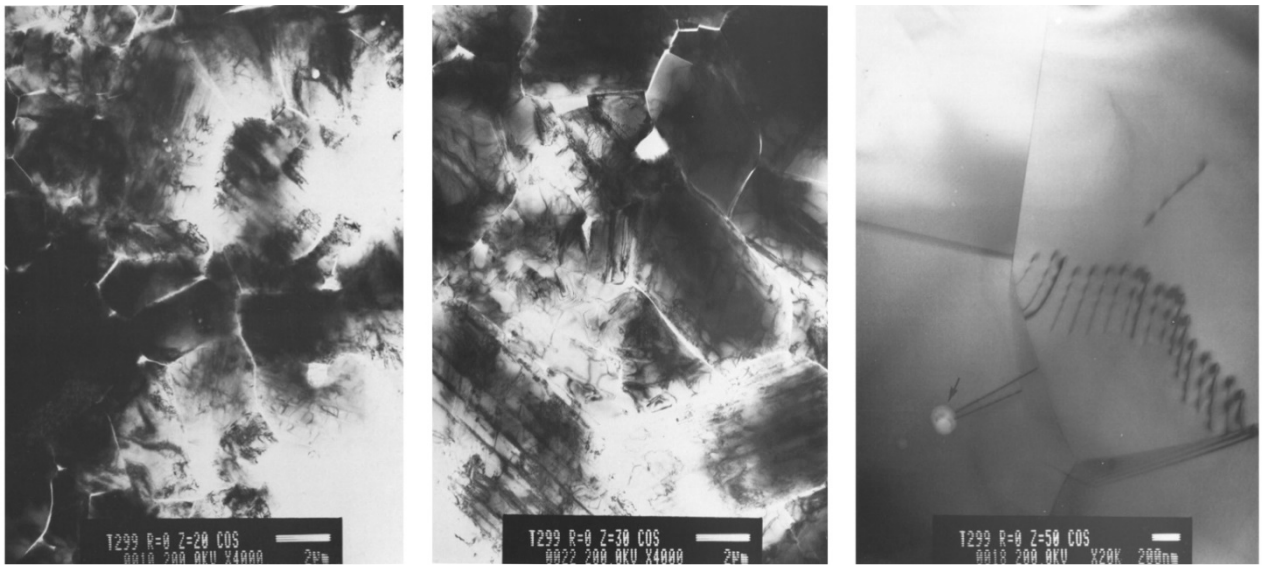


(a) (b) (c)

Figure 4.14 - TEM observations of fine-grained alumina recovered after a divergent spherical wave test. (a) *r* = 20 mm, (b) *r* = 30 mm, (c) *r* = 50 mm, the arrow indicates an intragranular pore.

### 4.4.5 Summary of damage modes observed in brittle materials as function of loading path.

A summary of damage modes observed in concrete samples subjected to different kinds of quasi-static and dynamic tests are depicted in the drawing of Figure 10 [question to PF: do you mean Figure 4.15?]. The loading paths are represented in a plot in which the horizontal axis corresponds to the hydrostatic pressure defined as function of the principal stresses ($\sigma_I,\ \sigma_{II},\ \sigma_{III}$):

$$P = -\frac{\sigma_I+\sigma_{II}+\sigma_{III}}{3}\ , \tag{11}$$

and the vertical axis corresponds to the Huber-Mises equivalent stress.

$$q = \sqrt{\frac{1}{2}[(\sigma_I-\sigma_{II})^2+(\sigma_{II}-\sigma_{III})^2+(\sigma_{III}-\sigma_I)^2]} \tag{12}$$

In this representation, the uniaxial compression test corresponds to a straight line starting from the origin of slope equal to 3. The oedometric path that corresponds to a compression in uniaxial strain ($\varepsilon_I = \varepsilon_{II} = 0,\ \varepsilon_{III} < 0$) is a straight line starting from the origin with a slope given by:

$$\frac{q}{P} = \frac{3(1-2\,\nu)}{1+\nu}\ , \tag{13}$$

where $\nu$ is the material's Poisson ratio. In a dynamic spalling test conducted with a Hopkinson bar apparatus radial and hoop stresses are supposed to be small compared to the axial stress and the slope in a (*P, q*) diagram would be equal to -3 for uniaxial tensile loading. Figure 4.15 indicates the expected damage modes as a function of the applied loading. Mode I multiple-fracturing is observed in spalling tests as well as in EOI tests far from the impact point (radius $r_2$). Mode II fracturing was observed in EOI tests in the vicinity of the dynamic confinement system (radius $r_1$). Pore collapse is anticipated under high confining pressures such as in triaxial tests, quasi-oedometric compression tests or within the confined area of EOI tests. Furthermore, the plot in Fig. 4.15 illustrates the strong increase of yield strength with pressure in concretes and their higher strain-rate sensitivity under tensile loading compared to confined compression loading. It is the reason why a constitutive model able to describe at the same time (i) the anisotropic damage due to mode I multiple fracturing in dynamic tensile loading, (ii) the pressure-dependent plastic yielding under high confining pressure and (iii) the plastic volumetric response due to irreversible collapse of pores is needed to numerically simulate the behaviour of a concrete structure subjected to hard-projectile impact. In the further section, a coupled plasticity-anisotropic damage model is presented to model the behaviour of concrete under dynamic tensile loading and confined compression.

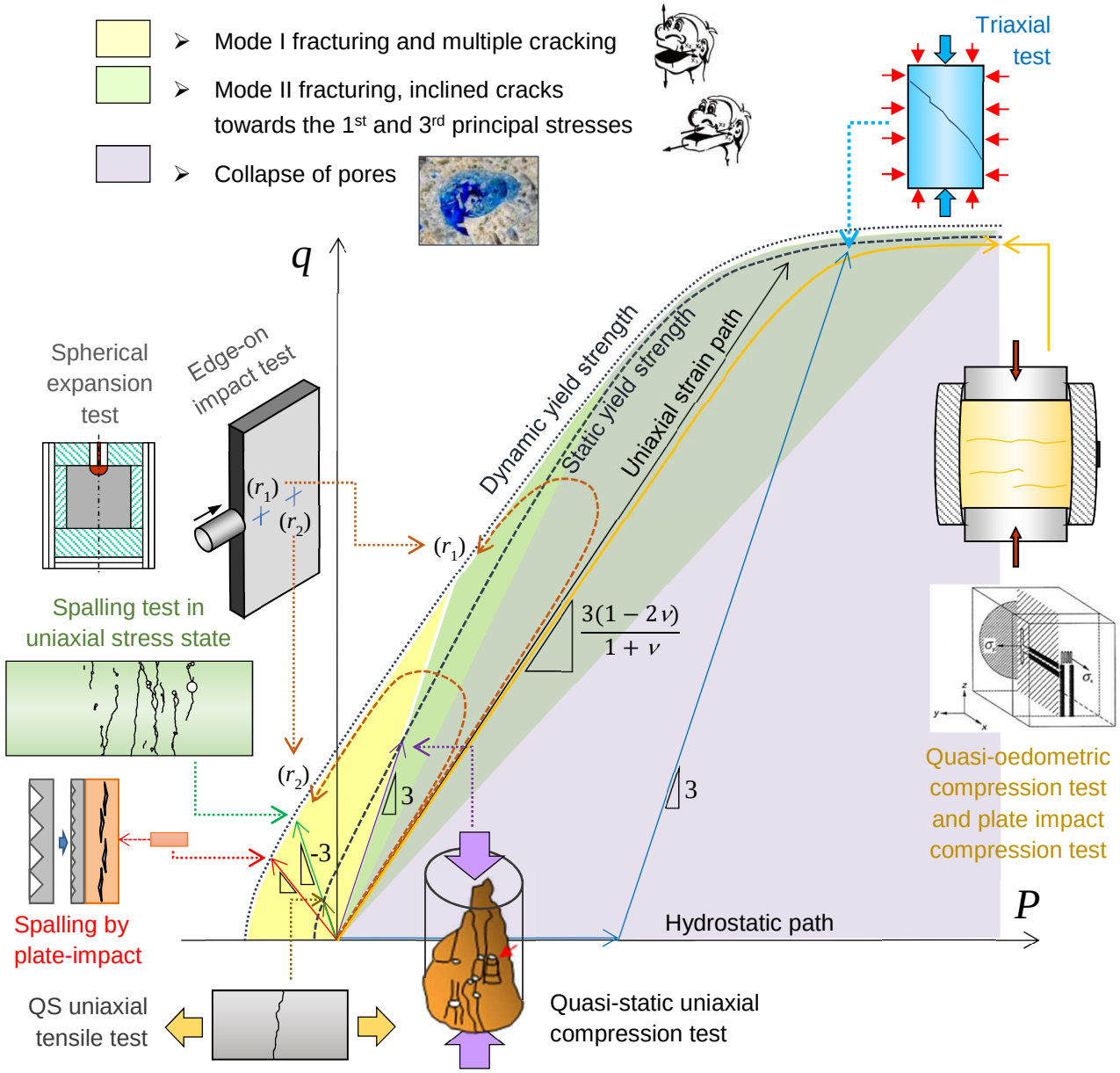


Figure 4.15 - Representation of the loading paths involved in various quasi-static and dynamic experiments applied to brittle materials. The areas in which mode I fracturing and multiple fragmentation, mode II fracturing (inclined cracks towards the 1st and 3rd principal stresses), micro-plasticity mechanisms (ceramics) and pore collapse (porous materials) are expected are depicted with different colors. Figure derived from (Forquin, 2021)

## 4.5 Micromechanics-based modelling of fragmentation process involved in brittle materials under high-rate tensile loadings

### 4.5.1 Introduction

For the last three decades, several analytical and numerical models have been proposed to describe and simulate the fragmentation process in brittle solids. Among them, energetic approaches provide analytical predictions of the fragments size distribution generated from dynamic loadings (Grady and Kipp, 1985), from which the spall strength strain-rate sensitivity of brittle solids can be deduced (Grady, 1988). This approach was coupled to a statistical distribution of fracture by Grady and Olsen (2003) for predicting the dynamic fragmentation of U6N rings. Based on an irreversible cohesive law, a cohesive model was proposed by Zhou et al (2005) to predict the one-dimensional fragmentation process by considering elastic wave propagation and equally-spaced or randomly-distributed point defect distribution. This approach allowed the fragment size distribution in a circular ring that is dynamically expanded to be predicted (Zhou et al, 2006). The dynamic fracture of brittle materials was numerically investigated considering element interfaces, therefore including parameters related to interfacial strength, fracture energy and crack opening. These approaches allowed the prediction of

fragmentation processes at a meso-scale (Camacho and Ortiz 1996, Espinosa et al, 1998; Maiti et al, 2005) even in a case of heterogeneous distribution of defects (Levy and Molinari, 2010). However, the main limitation of such approaches is that they have prohibitive calculation times, as they simulate a fragmentation process that involves up to a few tens of thousands of individual cracks generated in the loaded sample. In addition, parameters related to crack inception (linked to the flaw population) and crack propagation (crack speed) can be difficult to implement.
In parallel to discrete approaches, continuum damage models have been continuously developed to overcome these difficulties and better capture the physics of multiple-fragmentation induced in brittle materials due to the nucleation, growth and coalescence of multiple mode I cracks (Ravi-Chandar, 1998) or (in the case of biaxial compressive loading of a brittle material) uniformly distributed sliding cracks (Ravichandran and Subhash, 1995). Based on a continuum approach, Lu and Xu (2004) presented an isotropic damage model built on the concept of micro-crack nucleation, growth and coalescence. Even if this model is meant to describe micromechanical behaviours, it requires parameters identified from dynamic testing to properly describe the strain-rate sensitivity of concrete. However, the role of microstructural parameters remains insufficiently addressed in the literature. Whereas mesoscopic models constitute a possible way to account for microstructural properties, they present a number of drawbacks such as calculation costs, difficulties in parameter identification and validation procedure. An alternative is the development and implementation of so-called micromechanics-based models that rely on a description of the physical phenomenon involved in the macroscopic mechanical response of the solid of concern, as is the case in the Denoual, Forquin and Hild model.

### 4.5.2 Modelling of the fragmentation process through the concept of obscuration probability (the DFH Denoual-Forquin-Hild model)

The fragmentation process induced in brittle materials subjected to low or high strain-rates tensile loading corresponds to the initiation and propagation of a unique, a small or a large number of cracks from a volume or surface defects that originally exist in a structure Ω of size Z, with Z being a length, a surface area or a volume. The material flaws are assumed to be randomly distributed in space and activated at random levels of stress. The activation stress of each defect can be expressed as a function of its size, as considered by Jayatilaka and Trustrum (1977). The number of flaws in Z for which their activation stress is exceeded, named critical defects, can be represented through a density function corresponding to the number of critical defects for a given applied stress level $\lambda_t(\sigma)$. A schematic of a dynamic fragmentation process assuming that the stress level varies linearly or monotonically with time is presented in Fig. 4.16. The defects are distributed along the horizontal axis (spatial scale) and the vertical axis (representing the time-scale or stress-level scale). As the stress level rises ($\sigma^\circ > 0$), the number of activated defects increases. However, the first cracks that propagate from the first critical defects lead to the relaxation of tensile stresses in their neighbourhood ($\sigma^\circ < 0$). Such local stress release prevents the activation of any other critical defect in an "obscured domain" of size $Z_o(T - t)$ centred on the crack, where $T - t$ corresponds to the time interval between the crack inception $t$ and current $T$ times. The growth of obscuration domains (zones in which $\sigma^\circ < 0$) from activated defects is represented by triangles (obscuration hyper-cones) in Fig. 4.16, considering a constant speed for crack propagation. The fragmentation process ends when the whole domain is obscured.

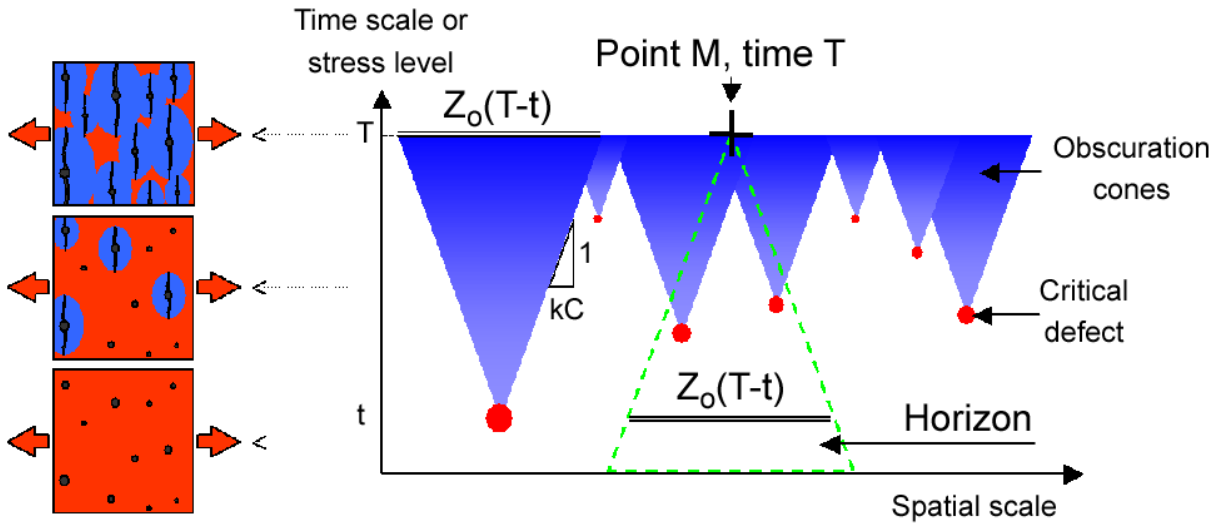


Figure 4.16 - Obscuration phenomenon and horizon of a point (*M*, *T* ).

The fragmentation process can be described by a probabilistic approach, by considering the condition for a point *M* at a time *T* not to be obscured. The condition of non-obscuration at a time *T* for a given flaw located at a point *M* may be expressed considering its past history: this condition is that no critical defect exists in its "horizon", the horizon being the space-time domain around (*M, T*) in which any crack will always obscure the point *M* at time *T*:

$$Horizon\ of\ (M,T) = \{\underline{x},t\} \in [Z_0(T-t) \cap \Omega] \tag{14}$$

Now the condition of non-obscuration of a point *M* at time *T* may be expressed in terms of probability by applying the "weakest-link hypothesis" to the space-time domain corresponding to its horizon: the probability of non-obscuration is equal

to the product of elementary probabilities of no-inception of new cracks $P_{\notin}^{i}$ in each elementary space-time zones (*dZ* x *dt*) of Ω belonging to the horizon of the point *M* at time *T*:

$$P_{no}(M,T) = \prod_{[Horizon\ of(M,T)\ \in\ \Omega]} P_{\notin}^{i} \tag{15}$$

If one assumes that the material contains point defects of density $\lambda_t$ (hypothesis of a Poisson point process of intensity $\lambda_t$), the elementary probability of no-inception of new crack $P_{\notin}^{i}$ in *dZ* x *dt* reads (Forquin, 2003):

$$P_{\notin}^{i}(\underline{x},t) = exp\left(-\frac{\partial\lambda_t(\underline{x},t)}{\partial t}dZdt\right) \tag{16}$$

Thus, the general form of the probability of non-obscuration $P_{no}$ of a point *M* at a time *T* reads (Forquin and Hild, 2010):

$$P_{no}(M,T) = exp\left(-\iint_{(\underline{x},t)\in[Horizon\ of(M,T)\ \in\ \Omega]}\frac{\partial\lambda_t(\underline{x},t)}{\partial t}dZdt\right) \tag{17}$$

In the particular case of a uniform stress field, the non-obscuration probability reads (Forquin and Hild, 2010):

$$P_{no}(T) = \underbrace{exp\left(-\int_{t_Z}^{T}\frac{d\lambda_t(t)}{dt}Z_o(T-t)dt\right)}_{Multiple\ fragmentation} \times \underbrace{exp\left(-Z\int_{0}^{t_Z}\frac{d\lambda_t(t)}{dt}dt\right)}_{Single\ fragmentation} \tag{18}$$

where $t_Z$ is the interacting time corresponding to the intersection between the horizon of (*M, T*) and the boundary of the whole domain of size $Z_\Omega$:

$$Z_\Omega \equiv Z_0(T - t_z) \tag{19}$$

At high strain rates multiple fragmentation occurs and the horizon of (*M, T*) is small compared to the size of the domain ($Z_\Omega$) (Fig. 4.17 left). Therefore, $t_Z$ tends to zero and the obscuration probability becomes the damage variable proposed by Denoual and Hild (2000) (left part of Eq. 18). On the other hand, at low strain rates, single fragmentation occurs and the interacting time $t_Z$ tends to the current time *T* (Fig. 4.17 right). Consequently, the obscuration probability tends to the failure probability proposed by Weibull (1939) (i.e. the right part of Eq. 18 corresponds to Eq. 4).

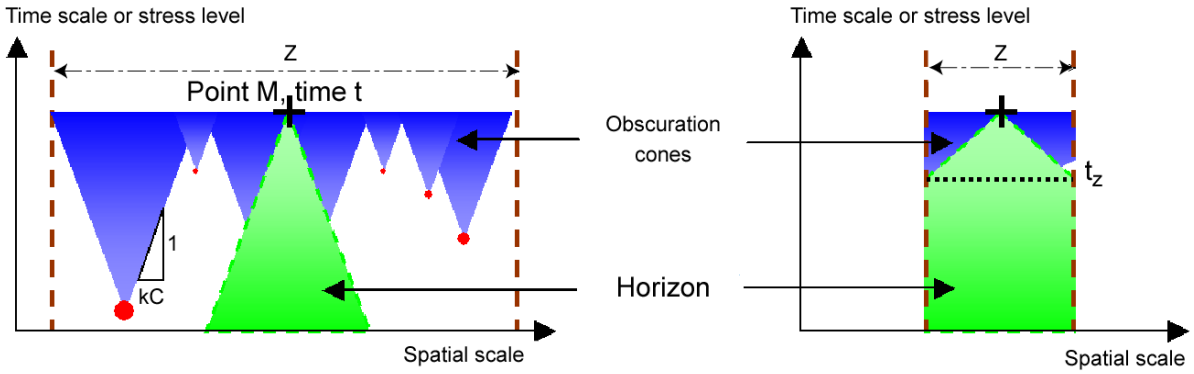


Figure 4.17 - Illustration of the influence of the relative sizes of the domain *Z* and the obscuration zones on the type of induced fragmentation. A large domain Z leads to a multiple fragmentation process (left) because the horizon of a point (*M, T* ) does not interact with the domain boundaries, whereas a small domain *Z* (right) leads to a single fragmentation process as the horizon of (*M, T* ) and the domain boundaries interact rapidly.

Now, the crack density $\lambda_{cracks}$ may be computed as a function of the obscuration probability $P_o$ and the increment of critical defects and considering that new cracks may emerge only in non-obscured zones (Denoual and Hild, 2000; Forquin and Hild, 2010):

$$\frac{\partial\lambda_{cracks}}{\partial t} = (1 - P_o)\ \frac{\partial\lambda_t}{\partial t} \tag{20}$$

Moreover, a damage variable may be defined in the framework of Continuum Damage Mechanics. By averaging over a representative zone, the obscuration probability $P_o$ is equivalent to an obscured volume fraction, with $P_o$ = 0 for the virgin material and $P_o$ = 1 for the fully obscured one and the macroscopic stress $\Sigma$ is computed from the obscuration probability and the microscopic stress:

$$\Sigma = \left(1 - \widetilde{D}\right)\sigma = (1 - P_o)\,\sigma + (P_o)^{\alpha_D}\sigma_{coh}(\varepsilon) \tag{21}$$

where $\sigma_{coh}(\varepsilon)$ corresponds to the residual strength (here called "cohesion strength") of the material despite the total obscuration of the domain Ω and $\alpha_D$ is an exponent set higher than 1 in order to reduce the influence of the cohesion strength $\sigma_{coh}(\varepsilon)$ at the stress peak. In the case of ceramics, this "cohesion strength" is usually assumed equal to zero. In the case of quasi-brittle materials like dry and wet concrete an empirical function of the cohesion strength was proposed by Erzar and Forquin (2014) to describe their softening behaviour:

$$\sigma_{coh}(\varepsilon) = \sigma_0^d\, exp\left(-\left(\frac{\varepsilon}{\varepsilon_0^d}\right)^{n^d}\right)\left(\frac{\dot{\varepsilon}}{\dot{\varepsilon}_0^{coh}}\right)^{\beta^d} + \sigma_0^w\, exp\left(-\left(\frac{\varepsilon}{\varepsilon_0^w}\right)^{n^w}\right)\left(\frac{\dot{\varepsilon}}{\dot{\varepsilon}_0^{coh}}\right)^{\beta^w}, \tag{22}$$

where $\sigma_0^d, \sigma_0^w, \varepsilon_0^d, \varepsilon_0^w, n^d, n^w, \beta_0^d, \beta_0^w, \dot{\varepsilon}_0^{coh}$ are material parameters to be identified. The first term of Eq. (22) describes the cohesion strength of a fully damaged dry concrete whereas the second one accounts for the additional strength of wet concrete induced by the presence of free water in open porosity and inside connected microcracks. Erzar and Forquin (2014) proposed considering the following exponents ($\beta^w = 0$; $\beta^d = n/(m+n)$ with $n = 3$ (and where $m$ is the Weibull modulus) to represent the strain-rate sensitivity of the cohesion strength of ordinary concrete. As shown by Erzar and Forquin (2014), because the ultimate strength (i.e. maximum macroscopic strength) is reached when $P_o$ is small ($P_o < 0.15$) the cohesion strength has a limited influence on the ultimate strength and the ultimate strength may therefore be approximated by:

$$\Sigma_u = \max_T[(1 - D(T))\sigma(T)] \approx \max_T[(1 - P_o(T))\sigma(T)] \tag{23}$$

### 4.5.3 Closed-form solution of DFH model in the case of a multiple-fragmentation

A closed-form solution of the obscuration probability (Eq. (18)), when a multiple fragmentation is described ($t_Z = 0$), can be expressed assuming that the density of critical flaws is expressed as a power law of the positive (tension) principal stress (Weibull distribution of critical defects given in Eq. 3) and considering that obscuration zones are growing in a self-similar way according to:

$$Z_o(T - t) = S\big(V_{crack}(T - t)\big)^n, \tag{24}$$

where $V_{crack}$ denotes the crack speed (assumed to be constant), $t$ corresponds to the time at which the crack initiates, $S$ is a shape parameter of the obscuration volume equal to 4π/3 when assuming that they are similar to spheres in a 3D medium ($n = 3$), π for a disk in a 2D medium ($n = 2$) and $S = 1$ in a 1D medium ($n = 1$). Now, one can compute the ultimate stress $\Sigma_u$ of the material by neglecting the cohesion strength of the material (Eq. 21) (Denoual and Hild, 2000):

$$\Sigma_u = \left(S_0\lambda_0^{-\frac{1}{m}}\right)^{\frac{m}{m+n}}\left(\dot{\sigma}\right)^{\frac{n}{m+n}}\left(S^{\frac{1}{n}}V_{crack}\right)^{-\frac{mn}{m+n}}\left(\frac{1}{e}\frac{(m+n-1)!}{m!\,n!}\right)^{\frac{1}{m+n}} \tag{25}$$

Moreover, based on previous simplifications (i.e. a constant stress rate along with an obscuration zone and a density of critical defects given by equations (24) and (3)) the final cracking density may be calculated by integrating Eq. (20):

$$\lambda_{cracks}^{T=\infty} = \left(S_0\lambda_0^{-\frac{1}{m}}\right)^{-\frac{mn}{m+n}}\left(\dot{\sigma}\right)^{\frac{mn}{m+n}}\left(S^{\frac{1}{n}}V_{crack}\right)^{-\frac{mn}{m+n}}\left(\frac{(m+n)!}{m!\,n!}\right)^{\frac{m}{m+n}}\Gamma\left(1 + \frac{m}{m+n}\right), \tag{26}$$

The predictions of the DFH model have been the subject of numerous comparisons with experimental results in terms of ultimate strength versus strain-rate (provided by spalling tests) and cracking density (provided for instance by post-mortem analysis of EOI tests). A few of them are presented in the next subsection.

### 4.5.4 Comparisons between DFH close-form solution and experimental results

EOI experiments in the sarcophagus configuration were conducted with four SiC ceramics (Forquin et al. 2018). The impacted targets were infiltrated post-test with a hyper fluid Epoxy resin before polishing for optical observations. Different sets of cracks are presented in Figure 4.18. The crack density ($\lambda_{cracks}^{T=\infty}$) was estimated at about 10 mm from the initial impact point for each grade by considering the mean distance ($d_{cracks}$) between parallel cracks according to the formula: $\lambda_{cracks}^{T=\infty} = 1/(d_{cracks})3$ (Forquin et al. 2018). In PS-S grade, the mean distance between cracks (0.21 mm) corresponds to a crack density of $1.0\text{x}10^{11}$ cracks/m$^3$. In SPS-S grade, the estimated crack density at 10 mm from the initial impact point is about $7.3\text{x}10^{10}$ cracks/m$^3$. In PS-L and SPS-L grades the crack densities are significantly lower being about $7.6\text{x}10^{9}$ cracks/m$^3$ and $4.2\text{x}10^{9}$ cracks/m$^3$ respectively.

A series of calculations were conducted with Abaqus Explicit Finite-Element code. The ceramic sample and the steel projectile were meshed with C3D8R elements (reduced integration) and the yield strength of the steel projectile was set to 1350 MPa. The impact velocity of the projectile was set to 170 m/s. The DFH anisotropic damage model was used to model the ceramic target. The parameters considered in the DFH model are reported in Table 4.1. The field of final cracking density (T = 7 µs) is illustrated in Figure 4.18 for each of the SiC ceramics and is compared to the post-mortem cracking pattern (Fig. 4.18). The numerical simulation enables the strong differences in cracking density (visualized in the fragmented targets) to be explained. Indeed, thanks to their lower Weibull modulus and higher average tensile strength, the SPS-L and PS-L ceramics generated a lower number of cracks and larger fragments than the PS-S and SPS-S grades.

Table 4.1 - Parameters of DFH model considered in the numerical simulation for the PS-S, SPS-S, PS-L and SPS-L SiC ceramics. Weibull parameters for the SPS-S, PS-L, SPS-L grades are provided from 4-point bending tests detailed in Rossiquet (2012). Weibull parameters for the PS-S grade are deduced from the results of 160 4-point bending tests provided by Saint-Gobain Research North America (NRDC) (Dargaud, 2021).

| Parameters: | PS-S | SPS-S | PS-L | SPS-L |
|---|---|---|---|---|
| Sample size (height x width x length) ($mm^3$) | 3 x 4 x 45 | 3 x 5 x 24 | | |
| Support and loading spans (mm) | 40, 20 | 20.8, 10 | | |
| Weibull modulus, $m$ | 14.0 | 13.3 | 5.1 | 7.9 |
| Effective volume, $V_{eff}$ ($mm^3$) | 8.5 | 5.6 | 14.5 | 9.5 |
| Mean tensile failure stress, $\sigma_w(V_{eff})$ (MPa) | 406 | 388 | 306 | 440 |
| Mean tensile failure stress for $V_{eff}$ = 1 $mm^3$ (MPa) | 473 | 442 | 517 | 585 |
| $K$, Shape parameter ($S$) | 0.38, 3.74 | | | |
| Young's modulus (GPa), Poisson's ratio | 410, 0.14 | | | |
| Density ($Kg/m^3$), 1D wave speed $C_0$ (m/s) | 3180, 11,535 | | | |

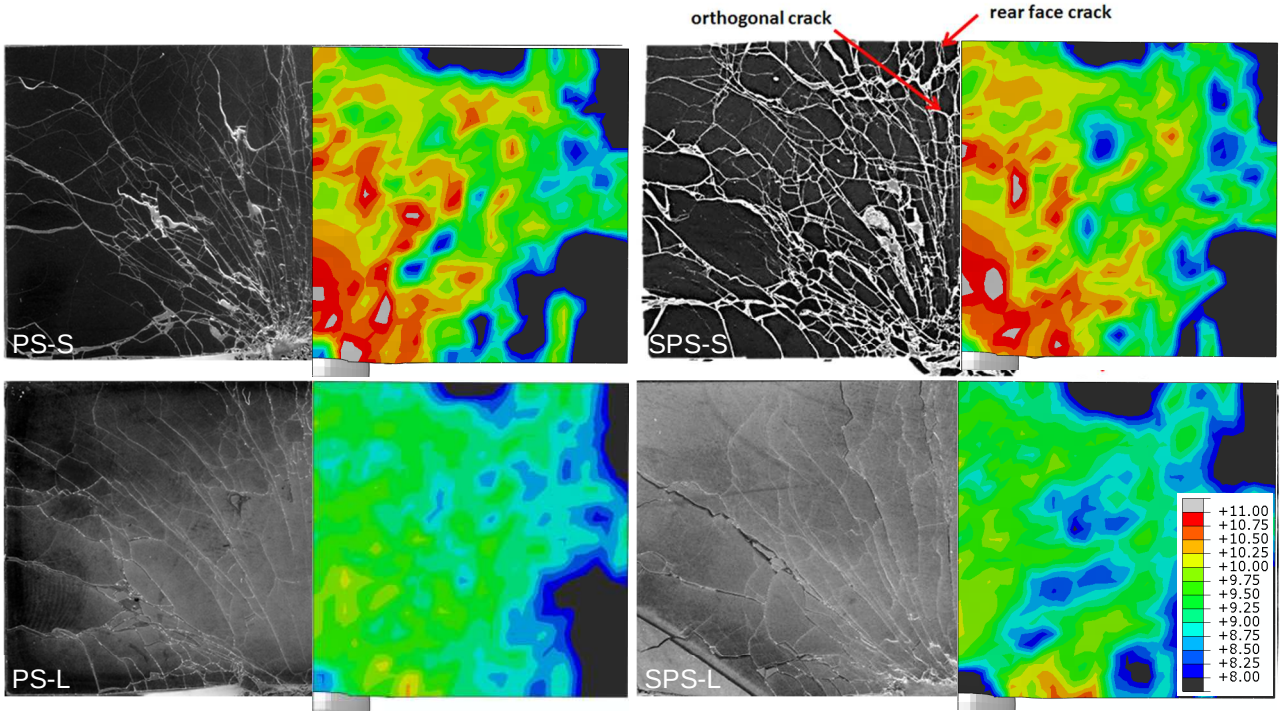


Figure 4.18 - Numerical simulation of the fragmentation process in PS-S, SPS-S, PS-L and SPS-L SiC ceramics subjected to EOI test (170 m/s) with DFH damage model. Isocontours of the final cracking density in log. scale ($m^{-3}$): for instance, $I$ = 9 would correspond to $10^9$ cracks per $m^3$ or 1 crack per $mm^3$ (Forquin et al, 2017; Forquin and Cosculluela, 2021)

### 4.5.5 Identification of the density of critical defects based on X-ray tomography CT-scan

In the framework of a research program called the Brittle's CODEX chair developed in the 3SR Laboratory (Forquin et al, 2020a; 2020b) two modelling approaches, called continuous and discrete methods, were developed to extend the domain of validity of the DFH model to a wider range of strain-rates (Forquin et al, 2021). Both approaches rely on a preliminary analysis of the existing flaw population by scanning virgin samples with X-ray micro-Computed Tomography (micro CT).
In a classical Weibull distribution of defects, the considered Weibull parameters are provided by a series of bending tests. The equivalent size of loaded volume refers to the effective volume provided by Davies (1973) (cf. Eq. (6)). It means that the Weibull parameters are valid in the case where the size of the loaded volume is close to the effective volume. However, their validity is questionable when the size of the loaded volume is much larger or smaller than the effective volume. This is an issue in the case of impact loading where strong stress gradients are generated leading to large range of crack

density within the considered volume. To solve this issue, it was proposed to identify the whole potential population of critical defects by using X-ray tomography CT-scan analysis (Fig. 4.19a).

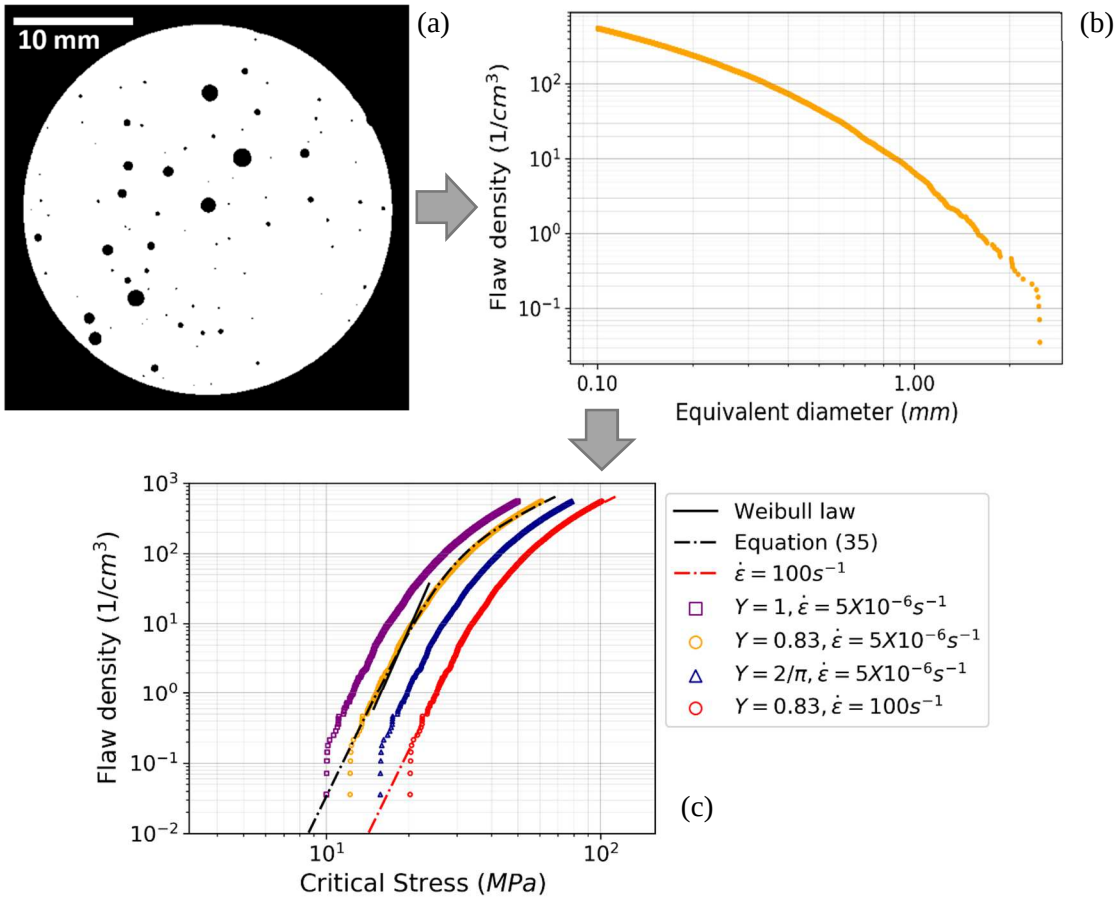


Figure 4.19 - (a) Slice of the binary 3D reconstructed image of X-ray micro-CT scan of a sample of Ultra-High-Performance Concrete (UHPC). (b) Cumulative flaw density plotted as a function of the flaw equivalent diameter $\lambda_t(D_{eq})$ (in log-log scale), (c) critical flaw density provided by tomographic analysis for three different values of the parameter $Y$ and interpolated function (black curved dash-dotted line) used in the continuous method. The Weibull flaws density provided by bending tests is plotted as a black solid straight line (Forquin et al, 2021).

In the work developed by Forquin et al (2021), the Linear Elastic Fracture Mechanics (LEFM) theory was used to link the size of pores to its expected crack-inception stress. According to this theory, the crack-inception stress of a crack of initial size ($D_{eq}$) is related to the critical stress intensity factor $K_{IC}$ according to the following equation:

$$\sigma_{trigger} = \frac{K_{IC}}{Y\sqrt{\pi D_{eq}/2}} \ , \tag{27}$$

where $Y$ is a dimensionless correction factor linked to the crack geometry, often referred to as the geometric shape factor and $K_{IC}$ is the critical stress intensity factor. For instance, in the case of a UHPC, Single-Edge Notched Bending (SENB) test reported in Forquin (2003) with a notched sample of UHPC (Ductal®) of dimensions 5×3×20 mm$^3$ ($h$×$w$×$L$, with $L$ the span length) provided the value $K_{IC}$ = 0.627 $MPa\sqrt{m}$. Next, by considering the cumulated density of critical defects provided by microtomography analysis, $\lambda_t(D_{eq})$ (Fig. 4.19b), the previous cumulated flaw density can be expressed as a function of the applied stress ($\sigma$):

$$\lambda_t(D_{eq}) = \lambda_t(D_{eq}(\sigma, Y, K_{IC})) \ \ with \ \ D_{eq} = \frac{2}{\pi}\left(\frac{K_{IC}}{Y.\sigma}\right)^2. \tag{28}$$

In Forquin et al (2021) the unknown parameter $Y$ is assumed to be constant whatever the size of the defects. This cumulated density of critical flaws is plotted for three different values of parameter $Y$ in Figure 4.19c. Moreover $Y$ can be identified from bending tests from which the Weibull scale parameter $\sigma_0(\lambda_0)^{-1/m}$ is deduced. Indeed, according to the Weibull theory the cumulated density of critical defects is expressed as Equation (3) (black solid straight line in Fig. 4.19c). By equalling Equations (28) and (3) at a stress equal to the mean bending failure stress determined in bending tests the parameter $Y$ is deduced ($Y = 0.83$) (Fig. 4.19c). Finally, an interpolated function (black curved dash-dotted line in Figure 4.19c) is used as input in the continuous method.

Furthermore, in the case of UHPC concrete a strain-rate sensitivity in the "quasi-static" regime was considered (Blasone et al, 2021), so the $\lambda_t$ curve varies with the applied strain rate as the crack-inception stress of the pores increases with the applied strain rate:

$$\sigma_{trigger}(\dot{\varepsilon}) = \sigma_{trigger}{}_0 \left(\frac{\dot{\varepsilon}}{\dot{\varepsilon}_0}\right)^{n_0}, \tag{29}$$

where $n_0$ corresponds to an exponent reflecting the strain-rate sensitivity in the "quasi-static" regime and $\dot{\varepsilon}_0$ is a reference strain-rate. This equation was considered by Forquin and Erzar (2010) and Erzar and Forquin (2014) to account for the strain-rate sensitivity of wet concrete tensile strength due to the presence of free-water (Rossi, 1991). According to the identification proposed in Blasone et al (2021), the following parameters were defined ($n_0 = 0.03$ and $\dot{\varepsilon}_0 = 5.10^{-6}$).

Next, the non-obscuration probability of the DFH model, expressed in Equation (8), can be rewritten by using the size of the obscuration zone proposed in Equation (24) (with $n = 3$), but without making any assumption about the density of critical defects $\lambda_t(\sigma(t))$, except that it is a continuous and derivable function. From the second derivative, the following differential equation is obtained (Denoual and Hild, 2000):

$$\frac{d^2}{dt^2}\left(\frac{1}{1-P_o}\frac{dP_o(T)}{dt}\right) = 6S(V_{crack})^3\lambda_t(\sigma(T)) \tag{30}$$

By applying a triple integration of this equation, the evolution of the obscuration probability can be determined over time for a given loading history $\sigma(t)$. Finally, the macroscopic stress and the ultimate macroscopic strength of the material (i.e. the maximum macroscopic stress) are deduced from Equation (21).

The model predictions in terms of ultimate strength were compared to experimental results from Blasone et al (2021) obtained through spalling experiments using a single Hopkinson bar apparatus in the plot of Figure 4.20. It is observed that the tensile strength given by the DFH model, using the Weibull power-law function and the defects population identified from tomography, are in good agreement with the experimental data at strain rates in the range of 50-200 $s^{-1}$.

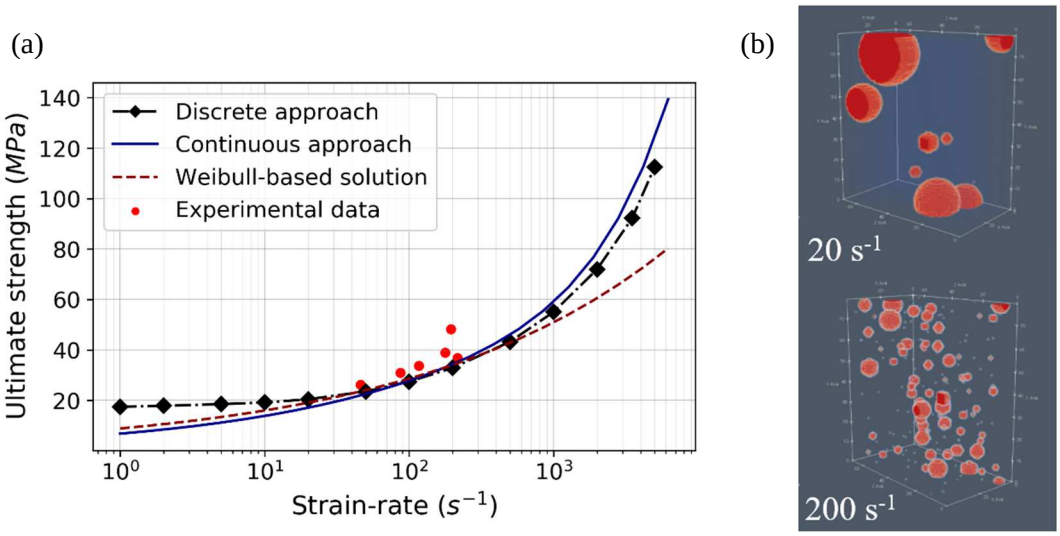


Figure 4.20 - (a) Predictions of the UHPC concrete macroscopic strength according to the applied strain-rate. Comparison between the DFH closed-form solution and the continuous and discrete methods, based on a Weibull flaw distribution and a flaw distribution identified from tomographic analysis, respectively. (b) Growing obscuration spheres from the discrete approach at 20 and 200 $s^{-1}$.

## 4.6 Micromechanics-based modelling of inelastic behaviour of brittle materials under confined compression

### 4.6.1 Introduction

Numerous plasticity models have been proposed and implemented in numerical codes to describe the behaviour of brittle materials, especially concrete, rocks or soils, under confined compression. Among them the Drucker-Prager (DP) model (1952) and the Krieg-Swenson-Taylor (KST) model (Krieg, 1978; Swenson et Taylor, 1983) are simple plasticity models used to describe the increase of yield strength with pressure. In addition, these models enable the description of the increase of volume with plastic strain (plastic dilation in the DP model) or the reduction of volume with the applied

hydrostatic pressure (compaction law in the KST model). These models have the advantage of being completely identifiable from triaxial compression tests. A perfectly hydrostatic compression test can give access to the compaction law (irreversible decrease of volume with pressure). However, in this case, the assumption is made that the hydrostatic behaviour will not be influenced by any shear deformation (decoupling or hydrostatic and deviatoric responses). However, these empirical models present several gaps. Indeed, they do not give any information about the possible role played by microstructural parameters (flaws, local friction, microcracking network…) and their predictive capabilities are limited (influence of loading path, case of non-proportional or non-monotonic loading…).

Micromechanics-based models may allow these gaps to be filled. These models aim to give a representation of micro-cracking processes involved in brittle materials under confinement which should give them good predictive capabilities. To do so, the damage process operating at a microscopic scale needs to be well understood. This was the goal of EOI tests performed on ultra-high strength concrete (Fig. 4.11). Their fine microstructure is optimal for accurate post-mortem observations. In addition, the cylindrical expansion loading that takes place in the target favours deviatoric (shear) deformation modes. In the target of Fig. 4.11, multiple cracking in mode II (cracks with rubbing lips) was observed with cracks starting from pores and propagating at an angle of about 45° towards the 1st and 3rd principal stresses. These observations look quite consistent with the failure process noted in Chen and Ravichandran (1997). These authors subjected ceramic samples confined by metal sleeves to axial compression. An inspection of the failure patterns in cross-sections revealed four stages of the conical fault formation process as schematically shown in Fig. 4.21. Growth of microcracks is observed until the peak strength is reached. Macrocracks then join to form a macroscopic crack in the softening stage. The final plateau corresponds to sliding of the fragments. This the phenomenology that needs to be reproduced by a micromechanics-based model.

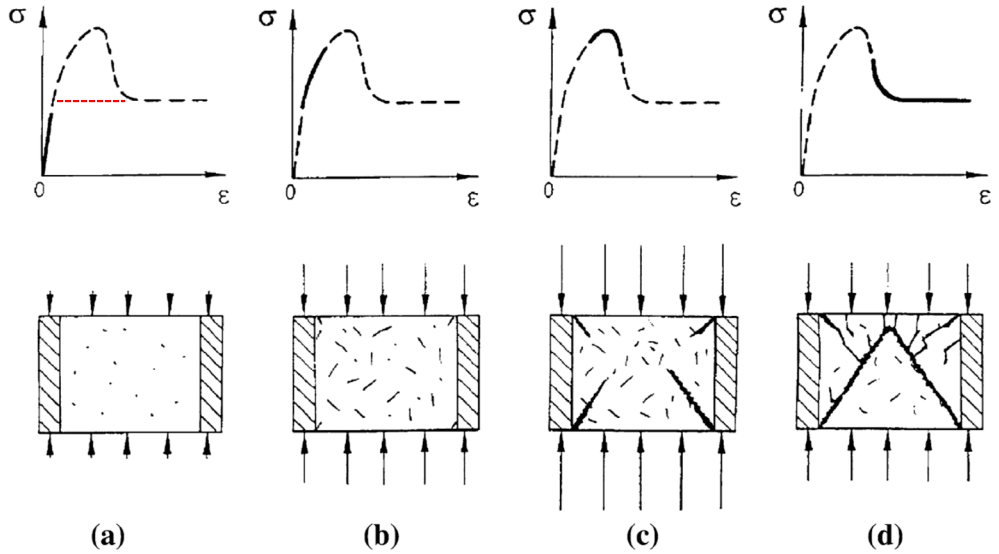


Figure 4.21 – Schematic of fracturing process induced in ceramics under confined compression. (a) elastic stage, (b) initial microcrack propagation, (c) Interaction of microcracks leading to macroscopic cracks initiated at the corners, (d) sliding of fragments (Chen et al. 2007).

## 4.6.2 Development of micromechanics-based models

The model proposed by Dragon and Mroz (1979) initiated a transition between plasticity and micromechanical models. It relies on a mechanical description of the behaviour of a pre-cracked cell. To the elastic strain is added a reversible strain associated with cracking, which plays the role of damage, and an irreversible strain due to plasticity. Each of these components has a corresponding yield surface F(σ) and f(σ), which may depend on the hydrostatic pressure, and a flow rule that may not respect the normality law (non-associated plasticity). The triaxial behaviour of geomaterials can be reproduced in this manner. This work was continued by Andrieux et al. (1986), Dragon et al. (1994), and Halm and Dragon, (1998) who all considered unilateral effects (crack reclosure) and sliding with friction at the crack lips.

For instance, Andrieux, et al (1986) proposed a two-dimensional square cell of side $l$ with a plane crack of length $2a$, normal $\underline{n}$, lower cracked face $\Gamma^-$ and upper cracked face $\Gamma^+$ (Fig. 4.22a). The crack orientation is assumed to be fixed. The state variables correspond to the variables that define the set of possible thermodynamic states of the cell. In addition to the observable variable (total macroscopic strain), internal variables are defined as the mean displacement jumps from either side of the crack lip ($\alpha$ and $\beta$) where $\alpha$ is the sliding variable and $\beta$ is the opening variable.

$$\alpha = \frac{1}{|\Omega|}\int_{\Gamma^+}[u_t] \quad \text{and} \quad \beta = \frac{1}{|\Omega|}\int_{\Gamma^+}[u_n] \qquad \text{(31) and (32)}$$

The modeling aims to distinguish in the mechanical response of the cracked cell the contribution generated by the loading applied to the non-cracked material from the contribution generated by the discontinuity of displacement on the

crack lips. The total strain tensor can be expressed as the sum of the elastic strain of the matrix (without crack) and the strain induced by $[u_t]$ and $[u_n]$.

$$\bar{\bar{E}} = \bar{\bar{E}}_m + \bar{\bar{E}}_d \quad \text{with} \quad \bar{\bar{E}}_m = (\bar{\bar{\bar{\bar{C}}}})^{-1}\bar{\bar{\Sigma}} \ , \qquad \text{(33) and (34)}$$

where $\bar{\bar{\bar{\bar{C}}}}$ is the elastic tensor of the non-cracked media and $\bar{\bar{\Sigma}}$ is the macroscopic stress tensor applied to the cell. By applying the virtual work principle to the cell, a link can be built between the internal variables of sliding and opening and $\bar{\bar{E}}_d$.

$$\bar{\bar{E}}_d = \alpha.sym\left(\underline{n}\otimes\underline{t}\right) + \beta\left(\underline{n}\otimes\underline{t}\right) \qquad (35)$$

The damage variable associated with crack length is defined as the area of influence of the crack $(2a)^2$ relative to the total area $l^2$:

$$d = 4\frac{a^2}{l^2} \ . \qquad (36)$$

Finally, the free energy corresponding to the elastic energy in the material can be expressed. This energy can be broken down into the energy that can be recovered by simple unloading (1st term) and the energy that is deemed irrecoverable (2nd term) and stored in elastic form via self-balancing of residual stresses present in the cell.

$$\psi = \frac{1}{2}\left(\bar{\bar{\bar{\bar{C}}}}.\bar{\bar{E}}_m\right):\bar{\bar{E}}_m + \frac{1}{2}K\left(\alpha^2 + \beta^2\right) \ , \qquad (37)$$

where $K$ is a parameter related to the elastic coefficients of the matrix and to the parameter $d$:

$$K = \frac{16\mu}{(1+\chi)d} \ , \qquad (38)$$

where $\chi = 3\text{-}4\nu$ in plane strain and $\chi = (3\text{-}\nu)/(1+\nu)$ in plane stress. This model was used to predict the response of cracked media under uniaxial tensile-compression loading, cyclic loading or biaxial loading. It provides a description of crack closure, hysteretic response and cyclic loadings, anisotropic behaviour as a function of crack orientation and residual strain under confinement.

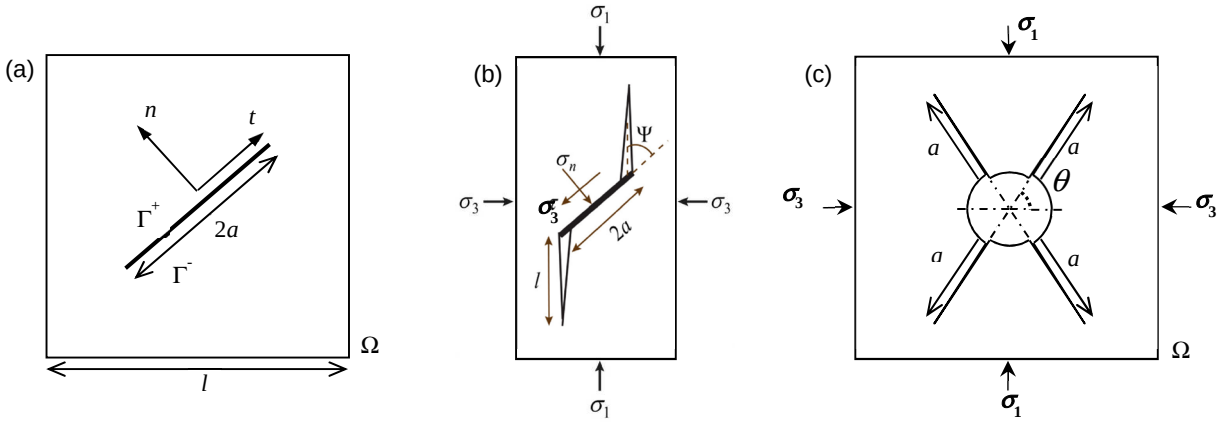


Figure 4.22 – Different elementary microcracked cell used to develop micro-mechanical model. (a) Microcracked cell proposed by Andrieux et al. (1986), (b) Microcracked cell proposed by Horii and Nemat-Nasser (1986), (c) Microcracked cell proposed by Forquin (2003).

Horii and Nemat-Nasser (1986) later proposed a micro-mechanical model based on a cell containing an inclined crack of length $c$, extended at each end by an axial crack and a slip band of the same inclination as the initial crack (Fig. 4.22b). Depending on the level of confinement, the authors predict axial cracking in mode I (brittle fracture) or sliding in mode II (ductile fracture). One parameter conditioning the brittle/ductile transition is $K_1^c/\sigma_y/(\pi c)^{1/2}$, which corresponds to the ratio between the energy required for the opening mode and the energy required for sliding ($c$ represents an inclined crack). This model has been validated in triaxial tests performed on silicate and carbonate rocks. Using the same cell, Ravichandran and Subhash (1995) constructed a single-variable damage model. A limit crack-speed was defined to explain the increase of compressive strength with the applied loading-rate.

In the work proposed by Forquin (2003) an elementary microcracked cell was designed with four cracks assumed to be triggered from a spherical pore and propagating along straight paths with an inclination angle $\theta$ defined towards the first and third macroscopic principal stresses (Fig. 4.22c). This angle was set to 45° based on observation made in Fig. 4.11. A mode II crack propagation mechanism with rubbing crack lips is assumed. Homogeneous displacement conditions at the outer surfaces ensure that the pattern is repeated ad infinitum. The cell is assumed to be loaded by different negative lateral and axial stresses ($\sigma_1 < 0$, $\sigma_3 < 0$) whereas the plane strain condition is used in direction 2. The crack propagation is assumed to be driven by the deviatoric stress $\sigma_{eq} = |\sigma_1 - \sigma_3|$ where $\sigma_1$ and $\sigma_3$ are the 1st and 3rd macroscopic principal stresses. The equivalent pressure is defined as the average value of principal stresses $\sigma_1$ and $\sigma_3$: $P = |\sigma_1 + \sigma_3|/2$.

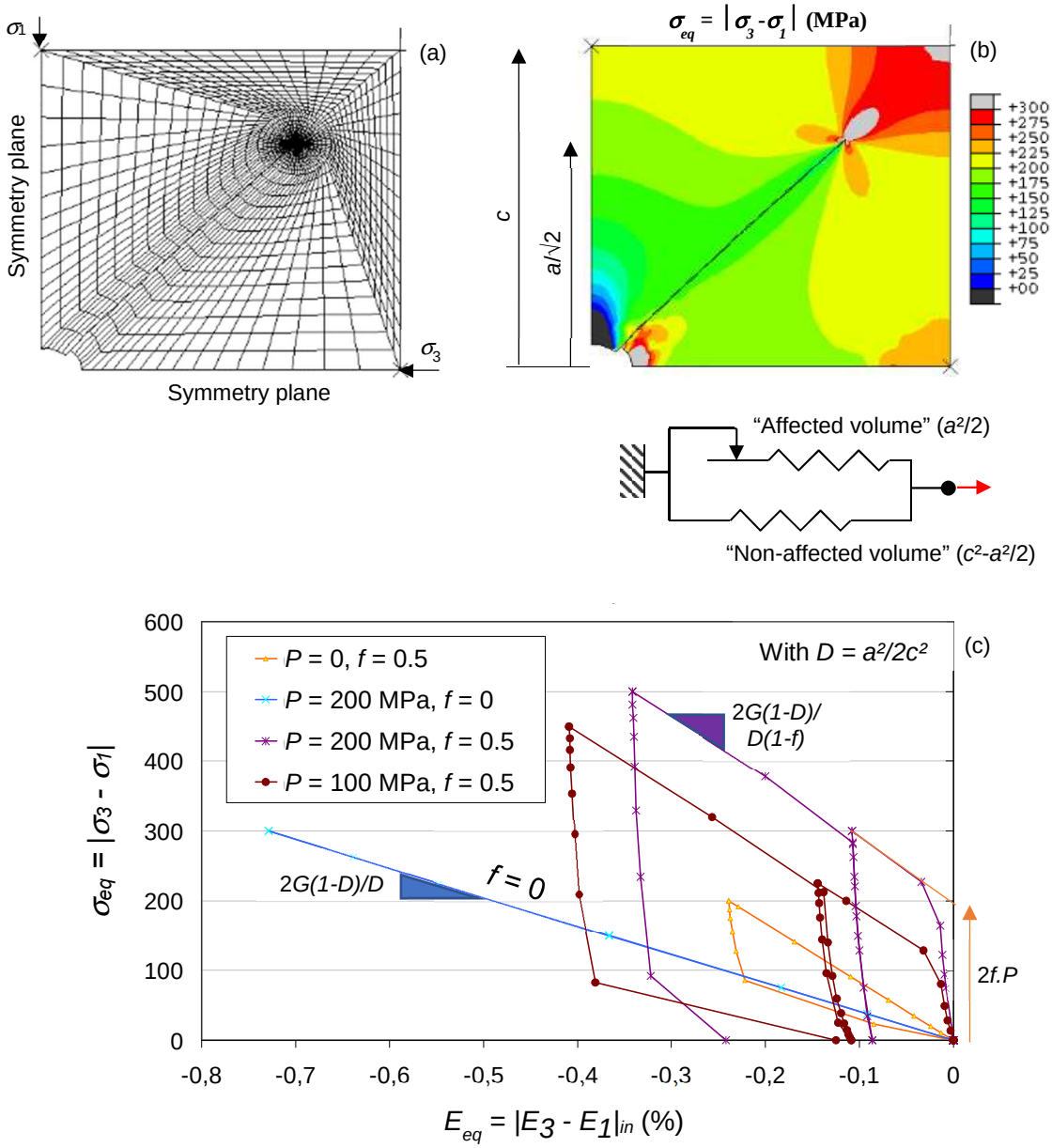


Figure 4.23 –Numerical response of an elementary cell subjected to triaxial loading in plane strain condition (Forquin, 2003). (a) Example of mesh used, (b) Equivalent stress field, (c) Mechanical response considering two different friction coefficients ($f$ = 0 or 0.5), three equivalent pressures ($P$ = 0, 100, 200 MPa) and $D$ = 0.5.

The elementary cell was the subject of numerical simulations, an example of which is shown in Fig. 4.23. The isocontours associated with the equivalent stress are plotted in figure 4.23b. The presence of the crack does indeed cause a reduction of the equivalent stress in an area of approximate size equal to $a^2/2$. The change of equivalent stress in this area is directly related to the friction coefficient and to the equivalent pressure applied. Calculations were made considering different friction coefficients ($f$ = 0 or 0.5), equivalent pressures ($P$ = 0, 100, 200 MPa) and $D$ = 0.5 (Fig. 4.23c). It reveals that the elastic yield strength is directly related to the friction coefficient and the equivalent pressure ($\sigma_{eq} = 2fP$). A plastic hardening response is noted with friction and pressure ($f > 0$). According to the model prediction the slower the crack growth the stronger the plastic hardening and the subsequent plastic softening. If the friction coefficient and pressure are kept constant the final residual strength tends to the initial elastic yield strength whatever the damage kinetics (which corresponds very well to the schematic representation provided in Fig. 4.21 cf. red dotted line).

On the other hand, without friction ($f = 0$) or pressure ($P = 0$) the elastic yield strength is zero and a damaged response is noted. Finally, by adjusting the friction and the kinetics of crack propagation, a coupled plasticity-damage model is generated including plastic-strain hardening, plastic-strain softening, residual strength, hysteretic response under cyclic loading and damage in the cases of low pressure or low friction. The contribution of this cell compared to the one presented previously (Fig. 4.22) also lies in the fact that since a defect exists at the origin of cracking, the defect population (porosity) can be linked to the cracking density and the kinetics of damage. However, the influence of defect population and limited crack speed still need to be further investigated.

In conclusion, micro-mechanical models based on micro-cracked cells enables the reproduction of numerous characteristics of the behaviour of brittle materials under confinement, without having to rely on phenomenological laws. In particular it provides a better understanding of the asymmetry between tension and compression, the reason for the dependence of strain-hardening and strain-softening on the confinement pressure, and the hysteresis observed in load/unload cycles. It can also be used to identify parameters such as cracking angle or friction coefficient by comparing analytical or numerical predictions with experimental data. This model also has certain imperfections or shortcomings, such as the adjustment of parameters related to crack initiation, or the difficulty of considering a change of crack orientation during its propagation. The effect of loading rate under confinement would merit to be better established and considered in the micro-mechanical model through an appropriate constitutive law driving the propagation of cracks in mode II for instance.

## 4.7 Conclusions

In conclusion, this chapter illustrates the variety and complexity of loadings and resulting damage modes induced in brittle materials subjected to intense loadings such as contact detonation or hard-projectile impact. Indeed, transient dynamic loadings are generated in the volume corresponding to short pulses (a few µs for instance in the case of tensile fracturing) or much longer continuous loadings (for instance about 1 ms for the whole penetration process) leading to specific damage modes such as microplasticity (dislocations, twinning, slip) and isotropic damage above the HEL (Hugoniot Elastic Limit) in ceramics, pore collapse and mode II fracturing in geomaterials under confined triaxial compression along with anisotropic damage in dynamic tension consisting in multiple oriented cracks, as observed in any kind of brittle materials.
These damage modes need to be carefully identified over a wide range of strain-rates (typically 10 $s^{-1}$ to $10^4$ $s^{-1}$) in order to better understand the influence of confinement and loading paths (hydrostatic, triaxial, shear, quasi-oedometric compression loading paths), the influence of strain-rate and the influence of microstructural parameters (flaws, pores, particles, free-water…) on the dynamic behaviour of brittle materials. To do so, specific experimental configurations such as the edge-on impact technique, shockless (GEPI or wavy-machined plate-impact) spalling tests or the pyrotechnic spherical expansion test can be used combined with time-resolved measurements (laser interferometry, PDV, pressure gauges, ultra-high-speed photography and full-field measurements…) or post-mortem analysis (SEM, TEM microscopy, CT-microtomography…). This wide variety of experimental data has led to a better understanding of damage mode at microscale (µm to nm) making it possible to develop more predictive models, such as the micromechanics-based model, in the form of analytical models or numerical representations. These approaches have enabled improvements in the description of the role plaid by microstructure (sintering flaws in ceramics, pores, aggregates, free water content in concrete…), thanks to a microtomography analysis of flaws populations in the Brittle's Codex chair, in view of extending the validity domain of the models over a much wider range of loadings and loading-rates. The development of a universal micromechanics-based model functioning whatever the applied loading and loading-rates, the considered scale and whatever the features of the microstructure under consideration still remains a strong prospect for further studies.

## Acknowledgments:

The author gratefully acknowledges the proofreading of the chapter by Dr. S. Walley and Dr. E. Buzaud.

## References:

Andrieux S., Bamberger Y., Marigo J.J. (1986) Un modèle de matériau microfissuré pour les bétons et les roches. J. Mécanique Théorique et Appliquée 5 (3), 471-513

Arias A., Forquin P., Zaera R. (2009) Impact damage in concrete targets subjected to perforation of high velocity metallic fragment. DYMAT 2009, 2009(2):1215–1221. DOI: 10.1051/dymat/2009171

Bischoff, P.H., Perry, S.H. (1991) Compressive behaviour of concrete at high strain rates. Materials and Structures 24, 425-450.

Cagnoux J. (1990) Spherical waves in pure alumina: Effects of grain size on flow and fracture, in Proceedings of the American Physical Society Topical Conference, Shock Compression of Condensed Matter, 1989, ed. by S.C. Schmidt, J.N. Johnson, L.W. Davidson, pp. 445-448, publ. Amsterdam, Elsevier.

Camacho G.T., Ortiz M. (1996) Computational modeling of impact damage in brittle materials. Int J Solids Struct., 33, 2899–2938.

Chen W.W., Rajendran A.M., Song B., Nie X. (2007) Dynamic fracture of ceramics in armor applications. J Am Ceram Soc 90(4), 1005–1018. doi:10.1111/j.1551-2916.2007.01515.x

Cosculluela A. (1992) Plasticité, endommagements et ruptures des alumines sous sollicitations dynamiques triaxiales : influence de la taille des grains (Ph.D. dissertation), University of Bordeaux, France.

Cosculluela, A., Forquin, P. (2021) Damage in Armor Ceramics Subjected to High-Strain-Rate Dynamic Loadings: The Spherical Expansion Shock Wave Pyrotechnic Test. In: Voyiadjis, G.Z. (eds) Handbook of Damage Mechanics. Springer, New York, NY. https://doi.org/10.1007/978-1-4614-8968-9_81-1

Dargaud M. (2021) Experimental and numerical analysis of the failure modes induced in ceramic materials under dynamic loading. (Ph.D. dissertation), Université Grenoble Alpes, France.
Dargaud M., Forquin P. (2021) A Shockless Plate-Impact Spalling Technique Based on Wavy-Machined Flyer-Plates to Evaluate the Strain-Rate Sensitivity of Ceramic Tensile Strength, J. Dynamic Behavior Mat., DOI: 10.1007/s40870-021-00317-4.
Davies, D.G.S. (1973) The Statistical Approach to Engineering Design in Ceramics. Proc. Brit. Ceram. Soc., 22, 429-452.
Dragon A., Mroz Z. (1979) A continuum model for plastic-brittle behaviour of rock and concrete. Int. J. Engrg. Sci. 17, pp. 121-137.
Dragon A., Cormery F., Desoyer T., Halm D. (1994) Localized failure analysis using damage models. Localization and Bifurcation Theory for Soils and Rocks, Rotterdam, Balkema, pp. 127-140.
Denoual C., Hild F. (2000) A damage model for dynamic fragmentation of brittle solids. Computer methods in Applied Mech. & Eng., 183:247-258.
Duplan Y., Forquin P. (2021) Investigation of the multiple-fragmentation process and post-fragmentation behaviour of dense and nacre-like alumina ceramics by means of tandem impact experiments and tomographic analysis, Int. J. Impact Eng., 155, 103891, DOI: 10.1016/j.ijimpeng.2021.103891.
Erzar B., Forquin P. (2011) Experiments and mesoscopic modelling of dynamic testing of concrete. Mech. Mat., 43 (9):505-527.
Erzar B., Forquin P. (2014) Analysis and modelling of the cohesion strength of concrete at high strain-rates. Int. J. Solids Structures, 51(14), 2559-2574. http://dx.doi.org/10.1016/j.ijsolstr.2014.01.023.
Espinosa H.D., Zavattieri P.D., Dwivedi S.K. (1998) A finite deformation continuum/discrete model for the description of fragmentation and damage in brittle materials. J. Mech. Phys. Solids, 46(10), 1909–1942.
Forquin P. (2003) Endommagement et fissuration de matériaux fragiles sous impact balistique, rôle de la microstructure. Ph.D. dissertation, Ecole Normale Supérieure de Cachan, France.
Forquin P., Tran L., Louvigné P-F., Rota L., Hild F. (2003) Effect of Aluminum Reinforcement on the Dynamic Fragmentation of SiC Ceramics. Int. J. Impact Eng., 28:1061-1076.
Forquin P., Arias A., Zaera R. (2006) An experimental method of measuring the confined compression strength of high-performance concretes to analyse their ballistic behaviour. J. Physique IV, 134:629-634. DOI: 10.1051/jp4:2006134097
Forquin P., Arias A., Zaera R. (2008) Role of Porosity in Controlling the Mechanical and Impact Behaviours of Cement-Based Materials. Int. J. Impact Eng., 35(3):133-146.
Forquin P., Hild F. (2008) Dynamic Fragmentation of an Ultra-High Strength Concrete during Edge-On Impact Tests. J. Eng. Mech., 134(4):302-315.
Forquin P., Erzar B. (2010) Dynamic fragmentation process in concrete under impact and spalling tests. Int. J. Fracture, 163:193-215.
Forquin P., Hild F. (2010) A probabilistic damage model of the dynamic fragmentation process in brittle materials. Advances in Applied Mech, Giessen & Aref Eds., 44:1-72. Academic Press, San Diego, CA.
Forquin, P. (2012) An optical correlation technique for characterizing the crack velocity in concrete. European Phys. J. – ST, 206(1):86-95.
Forquin P., Sallier L., Pontiroli C. (2015) A numerical study on the influence of free water content on the ballistic performances of plain concrete targets. Mech. Mat., 89:176-189.
Forquin P., Lukic B. (2016) Experimental Techniques to Characterize the Mechanical Behaviour of Ultra-High-Strength-Concrete Under Extreme Loading Conditions. In: *Song B., Lamberson L., Casem D., Kimberley J. (eds) Dynamic Behavior of Materials*, 1:229-237. DOI: 10.1007/978-3-319-22452-7_32.
Forquin P. (2017) Brittle materials at high-loading rates: an open area of research. Phil. Trans. R. Soc. A. 375(2085):20160436. DOI: 10.1098/rsta.2016.0436
Forquin P., Zinszner J.L., Lukic B. (2017) Mesoscopic Modelling of Ultra-High-Performance Fiber Reinforced Concrete Under Dynamic Loading. In: *Casem D., Lamberson L., Kimberley J. (eds) Dynamic Behavior of Materials*, 1:123-129, DOI: 10.1007/978-3-319-41132-3_17.
Forquin P., Zinszner J.-L., Rossiquet G., Erzar B. (2018) Microstructure influence on the fragmentation properties of dense silicon carbides under impact. Mech. Mat., 123:59-76.
Forquin P., Safa K., Gary G., 2010. Influence of free water on the quasi-static and dynamic strength of concrete in confined compression tests. Cement Concrete Res., 40(2), pp. 321-333.
Forquin P. (2015) Influence of Free Water and Strain-Rate on the Behaviour of Concrete Under High Confining Pressure. Chapter 40. In: Song B., Casem D., Kimberley J. (eds) Dynamic Behavior of Materials, Volume 1: Proceedings of the 2014 Annual Conference on Experimental and Applied Mechanics. The Society for Experimental Mechanics. Springer. pp 279-283.
Forquin P., Zinszner J.L. (2017) Experimental Study of the Dynamic Fragmentation in Transparent Ceramic Subjected to Projectile Impact. In: Casem D., Lamberson L., Kimberley J. (eds) Dynamic Behavior of Materials, Volume 1, pp 165-170, DOI: 10.1007/978-3-319-41132-3_23. Book series: Proceedings of the Society for Experimental Mechanics Series. Springer.
Forquin P., Blasone M., Georges D., Dargaud M. (2021) Continuous and discrete methods based on X-ray computed-tomography to model the fragmentation process in brittle solids over a wide range of strain-rates-application to three brittle materials, J. Mechanics and Physics of Solids, 152, 104412, DOI: 10.1016/j.jmps.2021.104412.
Forquin, P. (2021) Damage in Concrete Subjected to Impact Loading. In: Voyiadjis, G.Z. (eds) Handbook of Damage Mechanics. Springer, New York, NY. https://doi.org/10.1007/978-1-4614-8968-9_79-1
Forquin, P., Cosculluela, A. (2021) Damage in Armor Ceramics Subjected to High-Strain-Rate Dynamic Loadings: The Edge-on Impact Test. In: Voyiadjis, G.Z. (eds) Handbook of Damage Mechanics. Springer, New York, NY. https://doi.org/10.1007
Freudenthal, A.M. (1968) Statistical Approach to Brittle Fracture. In: Fracture, H. Liebowitz, Eds. Academic Press, New York (USA), vol. II. 591-619.
Gary G., Klepaczko J.R., Hamelin P., Rossi P. (1991) Résultats concernant le comportement dynamique en compression du microbéton. GRECO Géomatériaux. Rapport Scientifique, groupe 1, projet 1.3, "dynamique des bétons et des roches", 134-138.
Gorham, D.A. (1989) Specimen inertia in high strain-rate compression. J. Phys D Appl. Phys. 22, 1888-1893.
Grady D.E., Kipp M.E. (1985) Geometric statistics and dynamic fragmentation. J. Applied Physics, 58, 1210–1222.
Grady D.E. (1988) The spall strength of condensed matter. J. Mech. Physics Solids, 36(3):353–384.
Grady D.E., Olsen M.L. (2003) A statistics and energy based theory of dynamic fragmentation. Int. J. Impact Eng., 29, 293-306.
Gulino, R., and Phoenix, S.L. (1991). Weibull Strength Statistics for Graphite Fibres Measured from the Break Progression in a Model Graphite/Glass/Epoxy Microcomposite. J. Mater. Sci. 26 (11), 3107-3118
Grange S., Forquin P., Mencacci S., Hild F. (2008) On the dynamic fragmentation of two limestones using edge-on impact tests. Int. J. Impact Eng., 35:977-991.

Halm D., Dragon A. (1998) An isotropic model of damage and frictional sliding for brittle materials. Eur. J. Mech. A/Solids 17 (3), pp. 439-460.
Hoek, E., Franklin, J.A. (1968) A simple triaxial cell for field and laboratory testing of rock. Trans. Instn Min. Metall. 77, A22-26.
Heard H.A., Cline C.F. (1980) Mechanical Behaviour of Polycrystalline BeO, Al2O3 and AlN at High Pressure. J. Mater. Sci. 15, 1889-1897.
Horii H., Nemat-Nasser S. (1986) Brittle failure in compression: Splitting, faulting and brittle-ductile transition. Phil. Trans. R. Soc. Lond. 319, pp. 337-37
Jayatilaca A.D.S., Trustmm K. (1977) Statistical approach to brittle fracture. J. Mat. Sci., 12, 1426-1430.
Jeulin, D. (1991) Modèles morphologiques de structures aléatoires et changement d'échelle. thèse d'État, Université de Caen.
Kingery, W.D., Bowen, H.K., Uhlmann, D.R. (1976) Introduction to Ceramics. John Wiley and Sons, Inc., New York (USA).
Klepaczko, J.R., Brara, A. (2001) An experimental method for dynamic tensile testing of concrete by spalling. Int. J. Impact Eng. 25, 387-409.
Krieg R.D. (1978) A simple constitutive description for soils and crushable foams. Sandia National Laboratory, Report SC-DR-7260883.
Kutter, H.K., Fairhurst, C. (1971) On the Fracture Process in Blasting. Int. J. Rock Mech. Min. Sci. 8, 181-202.
Lankford, J. (1981) Temperature-strain rate dependence of compressive strength and damage mechanisms in aluminium oxide. J. Mater. Sci. 16, 1567-1578.
Lankford, J. (1991) The compressive strength of strong ceramics: microplasticity versus microfracture. J. Hard Materials 2 (1-2), 55-77.
Larson D.E. (1982) Explosively energy coupling in geologic materials. Int. J. Rock. Mech. Min. Sci. & Geomech. Abstr. 19, pp. 157-166
Leavy R.B., Clayton J.D., Strack O.E., Brannon R.M., Strassburger E. (2013) Edge on Impact Simulations and Experiments, Procedia Engineering, 58, 445–452.
Levy S., Molinari J.F. (2010) Dynamic fragmentation of ceramics, signature of defects and scaling of fragment sizes. J. Mech. Physics Solids, 58(1):12–26
Lu Y., Xu K. (2004) Modelling modelling of dynamic behaviour of concrete materials under blast loading. Int. J. Solids Struct., 41, 131–143.
Lukić B., Saletti D., Forquin P., Blasone M., Cohen A., Rack A. (2022) Single Bunch X-Ray Phase-Contrast Imaging of Dynamic Tensile Failure in Geomaterials. J. dynamic behavior mater. DOI: 10.1007/s40870-022-00350-x.
Malaise F. (1999). Réponse d'une céramique à l'impact d'un barreau à grande vitesse (1500 m/s). Croisement essais dynamiques-modélisation numérique. PhD thesis, Ecole Nationale Supérieure d'Arts et Métiers, Centre de Bordeaux, (in french).
Maiti S., Rangaswamy K., Geubelle P.H. (2005) Mesoscale analysis of dynamic fragmentation of ceramics under tension. Acta Mater., 53, 823–834.
McCauley J.W., Strassburger E., Patel P., Paliwal B., Ramesh K.T. (2013) Experimental Observations on Dynamic Response of Selected Transparent Armor Materials. Exp. Mech. 53(1), 3–29.
Palaniswamy, R., Shah, S.P. (1974) Fracture and stress– strain relationship of concrete under triaxial compression. J. Struct. Div. ASCE. ST5, 901–916.
Piotrowska E., Forquin P. (2015) Experimental investigation of the confined behavior of dry and wet high-strength concrete: quasi static versus dynamic loading. J. Dynamic Behavior Mat. 1 (2), 191-200.
Ravi-Chandar K. (1998) Dynamic fracture of nominally brittle materials. Int. J. Fract., 90, 83–102
Ravichandran G, Subhash G (1995) A micromechanical model for high strain rate behavior of ceramics. Int J Solids Struct, 32(17–18):2627–2646. doi:10.1016/0020-7683(94)00286-6
Riedel W., Hiermaier S., Thoma K. (2010) Transient stress and failure analysis of impact experiments with ceramics, Materials Science and Engineering B, 173, 139–147
Riou P., Denoual C., Cottenot C.E. (1998) Visualization of the damage evolution in impacted silicon carbide ceramics. Int. J. Impact Eng., 21(4), 225-235.
Rossi, P. (1988) Fissuration du béton: du matériau à la structure. Application de la mécanique linéaire de la rupture. Ph.D. dissertation. Ecole Nationale des Ponts et Chaussées, France.
Rossi, P. (1991) A physical phenomenon which can explain the material behaviour of concrete under high strain rates. Materials and Structures 24, 422-424.
Rossiquet G. (2012) Carbure de silicium pour application blindage : élaboration et étude du comportement à l'impact, (Ph.D. dissertation), Université de Bourgogne, France.
Saadati M., Forquin P., Weddfelt K., Larsson P.L., Hild F. (2017) On the mechanical behavior of granite material with particular emphasis on the influence from pre-existing cracks and defects. J. Testing and Evaluation, 46(1):20160072. DOI: 10.1520/JTE20160072.
Saadati M., Forquin P., Weddfelt K., Larsson P.L., Hild F. (2015) A numerical study of the influence of pre-existing cracks on granite rock fragmentation at percussive drilling. Num. Analytical Methods in Geomechanics, 39(5):558-570.
Saksala, T. (2010) Numerical Modelling of Rock Fracture in Percussive Drilling. PhD Thesis, Tampere University of Technology, Finland
Schuler, H., Mayrhofer, C., Thoma, K. (2006) Spall experiments for the measurement of the tensile strength and fracture energy of concrete at high strain rates. Int. J. Impact Eng. 32, 1635–1650.
Senf H., Strassburger E., Rothenhäusler H. (1994) Stress wave induced damage and fracture in impacted glasses, J. Phys. IV France, 04, C8-741-C8-746, DOI: 10.1051/jp4:19948114
Spanier, J., Oldham, K.B. (1987) An atlas of functions. Springer, New York (USA).
Strassburger E. (2004) Visualization of impact damage in ceramics using the edge-on impact technique, Int. J. Appl. Ceram. Technol. 1(3), 235–242
Swenson D.V., Taylor L.M. (1983) A finite element model for the analysis of tailored pulse stimulation of boreholes. Int. J. for Numerical and Analytical Methods in Geomechanics, 7:469-484.
Tonge A.L., Ramesh K.T. (2016) Multi-scale defect interactions in high-rate brittle material failure. Part I: Model formulation and application to ALON, J. Mech. Physics Solids, 86, 117–149.
Toutlemonde, F. (1994) Résistance au choc de structures en béton. Ph.D. dissertation. Ecole Nationale des Ponts et Chaussées.
Weibull, W. (1939) A Statistical Theory of the Strength of Materials. Report 151, Roy. Swed. Inst. Eng. Res.
Weibull, W. (1951) A Statistical Distribution Function of Wide Applicability. ASME J. Appl. Mech. 18 (3), 293-297.
Weerheijm, J. (1992) Concrete under impact tensile loading and lateral compression. Doctoral thesis, Delft University.
Wu, H., Zhang, Q., Huang, F., Jin, Q. (2005) Experimental and numerical investigation on the dynamic tensile strength of concrete. Int. J. Impact Eng. 32, 605–17.

Zhang G., Gazonas G.A., Bobaru F. (2018) Supershear damage propagation and sub-Rayleigh crack growth from edge-on impact: A peridynamic analysis, Int. J. Impact Eng. 113, 73–87.
Zhou F., Molinari J.-F., Ramesh K.T. (2005) A cohesive-model based fragmentation analysis: effects of strain rate and initial defects distribution, Int. J. Solids Structures, 42, 5181–5207.
Zhou F., Molinari J.-F., Ramesh K.T. (2006) Analysis of the brittle fragmentation of an expanding ring. Computational Materials Science, 37(1-2):74–85
Zinszner J-L, Forquin P, Rossiquet G (2015) Experimental and numerical analysis of the dynamic fragmentation in a SiC ceramic under impact. Int J Impact Eng 76:9–19
Zinszner J.-L., Erzar B., Forquin P. (2017) Strain-rate sensitivity of the tensile strength of two silicon carbides: experimental evidence and micromechanical modelling, Phil. Trans. R. Soc. A, 375(2085), 20160167